Cronfa - Swansea University Open Access Repository

_____

This is an author produced version of a paper published in :
IEEE Transactions on Visualization and Computer Graphics

_____

_____

Asymmetric Tensor Analysis
for Flow Visualization

Eugene Zhang, *Member, IEEE Computer Society*, Harry Yeh, Zhongzang Lin, and
Robert S. Laramee, *Member, IEEE Computer Society*

Abstract—The gradient of a velocity vector field is an asymmetric tensor field which can provide critical insight that is difficult to infer from traditional trajectory-based vector field visualization techniques. We describe the structures in the eigenvalue and eigenvector fields of the gradient tensor and how these structures can be used to infer the behaviors of the velocity field that can represent either a 2D compressible flow or the projection of a 3D compressible or incompressible flow onto a 2D manifold. To illustrate the structures in asymmetric tensor fields, we introduce the notions of *eigenvalue manifold* and *eigenvector manifold*. These concepts afford a number of theoretical results that clarify the connections between symmetric and antisymmetric components in tensor fields. In addition, these manifolds naturally lead to partitions of tensor fields, which we use to design effective visualization strategies. Moreover, we extend eigenvectors continuously into the complex domains which we refer to as pseudoeigenvectors. We make use of evenly spaced tensor lines following pseudoeigenvectors to illustrate the local linearization of tensors everywhere inside complex domains simultaneously. Both eigenvalue manifold and eigenvector manifold are supported by a tensor reparameterization with physical meaning. This allows us to relate our tensor analysis to physical quantities such as rotation, angular deformation, and dilation, which provide a physical interpretation of our tensor-driven vector field analysis in the context of fluid mechanics. To demonstrate the utility of our approach, we have applied our visualization techniques and interpretation to the study of the *Sullivan Vortex* as well as computational fluid dynamics simulation data.

Index Terms—Tensor field visualization, flow analysis, asymmetric tensors, flow segmentation, tensor field topology, surfaces.

✦

---

1 INTRODUCTION

Vector field analysis and visualization are an integral part of a number of applications in the field of aero- and hydrodynamics. Local fluid motions comprise transla- tion, rotation, volumetric expansion and contraction, and stretching. Most existing flow visualization techniques focus on the velocity vector field of the flow and have led to effective illustrations of the translational component. On the other hand, other flow motions may be the center of interest as well. For example, the stretching of fluids can be a good indicator for the rate of fluid mixing and energy dissipation, rotation expresses the amount of vorticity, and volumetric expansion and contraction are related to changes of fluid compressibility [2], [10], [24], [28]. The nontranslational components are directly related to the gradient tensor of the vector field. Consequently, inferring them using traditional vector field visualization methods that use arrows, streamlines, and colors encoding the

magnitude of the vector field (Figs. 1a, 1b, and 1c) is difficult even to trained fluid dynamics researchers.

The gradient tensor has found applications in a wide range of vector field visualization tasks such as fixed point classification and separatrix computation [12], attachment and separation line extraction [17], vortex core identification [29], [16], [25], [27], and periodic orbit detection [4]. However, the use of the gradient tensor in these applica- tions is often limited to point-wise computation and analysis. There has been relatively little work in investigat- ing the structures in the gradient tensors as a tensor field and what information about the vector field can be inferred from these structures. While symmetric tensor fields have been well explored, it is not clear how structures in symmetric tensor fields can be used to reveal structures in asymmetric tensor fields due to the existence of the antisymmetric components.

Zheng and Pang were the first to study the structures in 2D asymmetric tensor fields [40]. To our knowledge, this is the only work where the focus of the analysis is on asymmetric tensor fields. In their research, Zheng and Pang introduce the concept of *dual-eigenvectors* inside *complex domains* where eigenvalues and eigenvectors are complex. When the tensor field is the gradient of a vector field, Zheng and Pang demonstrate that dual-eigenvectors represent the elongated directions of the local linearization inside complex domains. Consequently, tensor field struc- tures can be visualized using a combination of eigenvectors and dual-eigenvectors.

The work of Zheng and Pang has inspired this study of asymmetric tensor fields. In particular, we address a number of questions that have been left unanswered. First, their algorithm for computing the dual-eigenvectors relies

- E. Zhang is with the School of Electrical Engineering and Computer Science, Oregon State University, 2111 Kelley Engineering Center, Corvallis, OR 97331. E-mail: zhange@eecs.oregonstate.edu.
- H. Yeh is with the College of Engineering, Oregon State University, 220 Owen Hall, Corvallis, OR 97331-3212. E-mail: harry@engr.orst.edu.
- Z. Lin is with the School of Electrical Engineering and Computer Science, Oregon State University, 1148 Kelley Engineering Center, Corvallis, OR 97331. E-mail: lin@eecs.oregonstate.edu.
- R.S. Laramee is with the Department of Computer Science, Swansea University, SA2 8PP, Wales, UK. E-mail: R.S.Laramee@swansea.ac.uk.
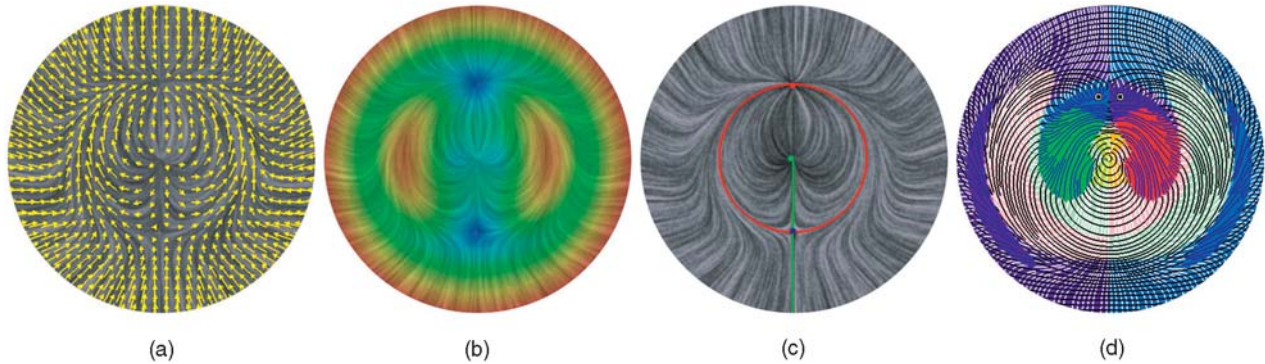
Fig. 1. The gradient tensor of a vector field (d) can provide additional information about the vector field that is difficult to extract from traditional vector field visualization techniques, such as (a) arrow plots, (b) trajectories and color coding of vector field magnitude, or (c) vector field topology [4]. The colors in (d) indicate the dominant flow motion (without translation) such as isotropic scaling, rotation, and anisotropic stretching. The tensor lines in (d) show the structures in the eigenvectors and dual-eigenvectors of the tensor, which reflect the directions of anisotropic stretching. Notice that it is a challenging task to use vector field visualization techniques (a)-(c) to provide insight such as locating stretching-dominated regions in the flow and identifying places where the orientations of the stretching change significantly. On the other hand, visualizations based on the gradient tensor (d) facilitate the understanding of these important questions. The detailed description for (d) will be discussed in Section 4.2. The flow field shown here is a planar slice of a 3D vector field that is generated by the linear superposition of two Sullivan Vortices with opposite orientations [30] (Section 5.1).

on eigenvector computation or singular value decomposition, neither of which provides much geometric intuition. Thus, a natural question is whether a more explicit relationship exists, and if so, what information about the vector field can be revealed from this relationship. Second, Zheng and Pang define *circular points* for asymmetric tensor fields that are the counterpart of degenerate points in symmetric tensors. While they provide a *circular discriminant* that can be used to detect circular points, it is not clear how to compute the tensor index of circular points, i.e., circular point classification (wedges, trisectors, etc.). Third, while dual-eigenvectors describe the elongation directions in the flow in complex domains, they cannot be used to visualize local linearization in the flow in those regions. Fourth, eigenvalues are an important aspect of tensor fields, yet there is little discussion on the structures of eigenvalues. Finally, their focus is on general asymmetric tensor fields, and there is limited investigation of the physical interpretation of their results in the context of flow analysis.

To address these fundamental issues, we make the following contributions:

1. We introduce the concepts of *eigenvalue manifold* (a hemisphere) and *eigenvector manifold* (a sphere), both of which facilitate tensor analysis (Section 4).

2. With the help of the eigenvector manifold, we extend the theoretical results of Zheng and Pang on eigenvector analysis (Section 4.1) by providing an explicit and geometric characterization of the dual-eigenvectors (Section 4.1.1), which enables degenerate point classification (Section 4.1.2).

3. We introduce pseudoeigenvectors, which we use to illustrate the elliptical flow patterns in the complex domains (Section 4.1.3).

4. We provide eigenvalue analysis based on a Voronoi partition of the eigenvalue manifold (Section 4.2), which allows us to maintain the relative strengths among the three main nontranslational flow components: isotropic scaling (dilation), rotation (vorticity), and anisotropic stretching (angular deformation).

This partition also demonstrates that direct transitions between certain dominant-to-dominant components are impossible, such as between clockwise and counterclockwise rotations. The transition must go through a dominant flow pattern other than rotation.

5. We present a number of novel vector and tensor field visualization techniques based on our eigenvalue and eigenvector analysis (Sections 4.1 and 4.2).

6. We provide physical interpretation of our analysis in the context of flow visualization (Section 5).

The remainder of the article is organized as follows: We will first review related existing techniques in vector and tensor field visualization and analysis in Section 2 and provide relevant background on symmetric and asymmetric tensor fields in Section 3. Then, in Section 4, we describe our analysis and visualization approaches for asymmetric tensor fields defined on 2D manifolds. We provide some physical intuition about our approach and demonstrate the effectiveness of our analysis and visualization by applying them to the Sullivan Vortex as well as cooling jacket and diesel engine simulation applications in Section 5. Finally, we summarize our work and discuss some possible future directions in Section 6.

2 PREVIOUS WORK

There has been extensive work in vector field analysis and flow visualization [20], [21]. However, relatively little work has been done in the area of flow analysis by studying the structures in the gradient tensor, an asymmetric tensor field. In general, previous work is limited to the study of symmetric second-order tensor fields. Asymmetric tensor fields are usually decomposed into a symmetric tensor field and a rotational vector field and then visualized simultaneously (but as two separate fields). In this section, we review related work in symmetric and asymmetric tensor fields.

2.1 Symmetric Tensor Field Analysis and Visualization

Symmetric tensor field analysis and visualization have been well researched for both two and three dimensions. To refer

to all past work is beyond the scope of this article. Here, we will only refer to the most relevant work.

Delmarcelle and Hesselink [7] provide a comprehensive study on the topology of 2D symmetric tensor fields and define *hyperstreamlines* (also referred to as *tensor lines*), which they use to visualize tensor fields. This research is later extended to analysis in three dimensions [13], [39], [41] and topological tracking in time-varying symmetric tensor fields [31].

Zheng and Pang provide a high-quality texture-based tensor field visualization technique, which they refer to as *HyperLIC* [38]. This work adapts the idea of *Line Integral Convolution (LIC)* of Cabral and Leedom [3] to symmetric tensor fields. Zhang et al. [36] develop a fast and high-quality texture-based tensor field visualization technique, which is a nontrivial adaptation of the *Image-Based Flow Visualization (IBFV)* of van Wijk [34]. Hotz et al. [15] present a texture-based method for visualizing 2D symmetric tensor fields. Different constituents of the tensor field corresponding to stress and strain are mapped to visual properties of a texture, emphasizing regions of volumetric expansion and contraction.

To reduce the noise and small-scale features in the data and, therefore, enhance the effectiveness of visualization, a symmetric tensor field is often simplified either geometrically through Laplacian smoothing of tensor values [1], [36] or topologically using degenerate point pair cancellation [32], [36] and degenerate point clustering [33].

We also note that the results presented in this article exhibit some resemblance to those using *Clifford Algebra* [9], [14], [8], in which vector fields are decomposed into different local patterns, e.g., sources, sinks, and shear flows, and then color-coded.

2.2 Asymmetric Tensor Field Analysis and Visualization

Analysis of asymmetric tensor fields is relatively new in visualization. Zheng and Pang provide analysis on 2D asymmetric tensors [40]. Their analysis includes the partition of the domain into real and complex, defining and use of dual-eigenvectors for the visualization of tensors inside complex domains, incorporation of degenerate curves into tensor field features, and a circular discriminant that enables the detection of degenerate points (circular points).

In this article, we extend the analysis of Zheng and Pang by providing an explicit formulation of the dual-eigenvectors, which allows us to perform degenerate point classification and extend the Poincaré-Hopf theorem to 2D asymmetric tensor fields. We also introduce the concepts of pseudoeigenvectors, which can be used to illustrate the elliptical patterns inside complex domains. Such an illustration cannot be achieved through the visualization of dual-eigenvectors. Moreover, we provide the analysis on the eigenvalues, which we incorporate into visualization. Finally, we provide an explicit physical interpretation of our analysis in the context of flow semantics.

Ruetten and Chong [26] describe a visualization framework for 3D flow fields that utilizes the three *principle invariants* P, Q, and R. Similar to our approach, they normalize the three quantities. On the other hand, for 2D flow fields as in our case, $Q = -R$. Therefore, their approach would only have two independent variables while, in our method, there are still three variables.

3 BACKGROUND ON TENSOR FIELDS

We first review some relevant facts about tensor fields on 2D manifolds. An asymmetric tensor field T for a manifold surface $\mathbf{M}$ is a smooth tensor-valued function that associates with every point $\mathbf{p} \in \mathbf{M}$ a second-order tensor

$$T(\mathbf{p}) = \begin{pmatrix} T_{11}(\mathbf{p}) & T_{12}(\mathbf{p}) \\ T_{21}(\mathbf{p}) & T_{22}(\mathbf{p}) \end{pmatrix}$$

under some local coordinate system in the tangent plane at $\mathbf{p}$. The entries of $T(\mathbf{p})$ depend on the choice of the coordinate system. A tensor $[T_{ij}]$ is *symmetric* if $T_{ij} = T_{ji}$.

3.1 Symmetric Tensor Fields

A symmetric tensor T can be uniquely decomposed into the sum of its isotropic part D and the (*deviatoric tensor*) A:

$$D + A = \begin{pmatrix} \frac{T_{11}+T_{22}}{2} & 0 \\ 0 & \frac{T_{11}+T_{22}}{2} \end{pmatrix} + \begin{pmatrix} \frac{T_{11}-T_{22}}{2} & T_{12} \\ T_{12} & \frac{T_{22}-T_{11}}{2} \end{pmatrix}. \quad (1)$$

T has eigenvalues $\gamma_d \pm \gamma_s$ in which $\gamma_d = \frac{T_{11}+T_{22}}{2}$ and

$$\gamma_s = \frac{\sqrt{(T_{11} - T_{22})^2 + 4T_{12}^2}}{2} \geq 0.$$

Let $E_1(\mathbf{p})$ and $E_2(\mathbf{p})$ be unit eigenvectors that correspond to eigenvalues $\gamma_d + \gamma_s$ and $\gamma_d - \gamma_s$, respectively. E_1 and E_2 are the *major* and *minor* eigenvector fields of T. $T(\mathbf{p})$ is equivalent to two orthogonal eigenvector fields: $E_1(\mathbf{p})$ and $E_2(\mathbf{p})$ when $A(\mathbf{p}) \neq 0$. Delmarcelle and Hesselink [6] suggest visualizing *tensor lines*, which are curves that are tangent to an eigenvector field everywhere along its path.

Different tensor lines can only meet at degenerate points, where $A(\mathbf{p}_0) = 0$ and major and minor eigenvectors are not well defined. The most basic types of degenerate points are: *wedges* and *trisectors*. Delmarcelle and Hesselink [6] define a *tensor index* for an isolated degenerate point $\mathbf{p}_0$, which must be a multiple of $\frac{1}{2}$ due to the sign ambiguity in tensors. It is $\frac{1}{2}$ for a wedge, $-\frac{1}{2}$ for a trisector, and 0 for a regular point. Delmarcelle shows that the total indices of a tensor field with only isolated degenerated points is related to the topology of the underlying surface [5]. Let $\mathbf{M}$ be a closed orientable manifold with an Euler characteristic $\chi(\mathbf{M})$, and let T be a continuous symmetric tensor field with only isolated degenerate points $\{\mathbf{p}_i : 1 \leq i \leq N\}$. Denote the tensor index of $\mathbf{p}_i$ as $I(\mathbf{p}_i, T)$. Then,

$$\sum_{i=1}^{N} I(\mathbf{p}_i, T) = \chi(\mathbf{M}). \quad (2)$$

In this article, we will adapt the classification of degenerate points of symmetric tensor fields to asymmetric tensor fields.

3.2 Asymmetric Tensor Fields

An asymmetric tensor differs from a symmetric one in many aspects, the most significant of which is perhaps that an asymmetric tensor can have complex eigenvalues for

which no real-valued eigenvectors exist. Given an asymmetric tensor field T, the domain of T can be partitioned into *real domains* (real eigenvalues λ_i where $\lambda_1 \neq \lambda_2$), *degenerate curves* (real eigenvalues λ_i where $\lambda_1 = \lambda_2$), and *complex domains* (complex eigenvalues). Degenerate curves form the boundary between the real domains and complex domains.

In the complex domains where no real eigenvectors exist, Zheng and Pang [40] introduce the concept of *dual-eigenvectors*, which are real-valued vectors and can be used to describe the elongated directions of the elliptical patterns when the asymmetric tensor field is the gradient of a vector field. The dual-eigenvectors in the real domains are the bisectors between the major and minor eigenvectors. The following equations characterize the relationship between the dual-eigenvectors J_1 (major) and J_2 (minor) and the eigenvectors E_1 (major) and E_2 (minor) in the real domains,

$$E_1 = \sqrt{\mu_1}J_1 + \sqrt{\mu_2}J_2, \quad E_2 = \sqrt{\mu_1}J_1 - \sqrt{\mu_2}J_2, \quad (3)$$

as well as in the complex domains,

$$E_1 = \sqrt{\mu_1}J_1 + i\sqrt{\mu_2}J_2, \quad E_2 = \sqrt{\mu_1}J_1 - i\sqrt{\mu_2}J_2, \quad (4)$$

where μ_1 and μ_2 are the singular values in the singular value decomposition. Furthermore, the following fields:

$$V_i(\mathbf{p}) = \begin{cases} E_i(\mathbf{p}) & T(\mathbf{p}) \text{ in the real domain,} \\ J_1(\mathbf{p}) & T(\mathbf{p}) \text{ in the complex domain,} \end{cases} \quad (5)$$

$i = 1, 2$ are continuous across degenerate curves. Either field can be used to visualize the asymmetric tensor field.

Dual-eigenvectors are undefined at *degenerate points*, where the *circular discriminant*,

$$\Delta_2 = (T_{11} - T_{22})^2 + (T_{12} + T_{21})^2, \quad (6)$$

achieves a value of zero. Degenerate points represent locations where flow patterns are purely circular, and they only occur inside complex domains. They are also referred to as *circular points* [40], and together with degenerate curves, they form the *asymmetric tensor field features*.

In this article, we extend the aforementioned analysis of Zheng and Pang [40] in several aspects that include a geometric interpretation of the dual-eigenvectors (Section 4.1.1), the classification of degenerate points and the extension of the Poincaré-Hopf theorem from symmetric tensor fields (2) to asymmetric tensor fields (Section 4.1.2), the introduction and use of *pseudoeigenvectors* for the visualization of tensor structures inside complex domains (Section 4.1.3), and the incorporation of eigenvalue analysis (Section 4.2).

4 ASYMMETRIC TENSOR FIELD ANALYSIS AND VISUALIZATION

Our asymmetric tensor field analysis starts with a parameterization for the set of 2×2 tensors.

It is well known that any second-order tensor can be uniquely decomposed into the sum of its symmetric and antisymmetric components, which measure the scaling and rotation caused by the tensor, respectively. Another popular decomposition removes the trace component from a

symmetric tensor which corresponds to isotropic scaling (1). The remaining constituent, the *deviatoric tensor*, has a zero trace and measures the anisotropy in the original tensor. We combine both decompositions to obtain the following unified parameterization of the space of 2×2 tensors:

$$T = \gamma_d \begin{pmatrix} 1 & 0 \\ 0 & 1 \end{pmatrix} + \gamma_r \begin{pmatrix} 0 & -1 \\ 1 & 0 \end{pmatrix} + \gamma_s \begin{pmatrix} \cos\theta & \sin\theta \\ \sin\theta & -\cos\theta \end{pmatrix}, \quad (7)$$

where $\gamma_d = \frac{T_{11}+T_{22}}{2}$, $\gamma_r = \frac{T_{21}-T_{12}}{2}$, and

$$\gamma_s = \frac{\sqrt{(T_{11} - T_{22})^2 + (T_{12} + T_{21})^2}}{2}$$

are the *strengths* of isotropic scaling, rotation, and anisotropic stretching, respectively. Note that $\gamma_s \geq 0$, while γ_r and γ_d can be any real number. $\theta \in [0, 2\pi)$ is the angular component of the vector

$$\begin{pmatrix} T_{11} - T_{22} \\ T_{12} + T_{21} \end{pmatrix},$$

which encodes the orientation of the stretching.

In this article, we focus on how the relative strengths of the three components effect the eigenvalues and eigenvectors in the tensor. Given our goals, it suffices to study *unit tensors*, i.e., $\gamma_d^2 + \gamma_r^2 + \gamma_s^2 = 1$.

The space of unit tensors is a 3D manifold for which direct visualization is formidable. Fortunately, the eigenvalues of a tensor only depend on γ_d, γ_r, and γ_s, while the eigenvectors depend on γ_r, γ_s, and θ. Therefore, we define the *eigenvalue manifold* $\mathbf{M}_\lambda$ as

$$\{(\gamma_d, \gamma_r, \gamma_s) \mid \gamma_d^2 + \gamma_r^2 + \gamma_s^2 = 1 \text{ and } \gamma_s \geq 0\}, \quad (8)$$

and the *eigenvector manifold* $\mathbf{M}_v$ as

$$\{(\gamma_r, \gamma_s, \theta) \mid \gamma_r^2 + \gamma_s^2 = 1 \text{ and } \gamma_s \geq 0 \text{ and } 0 \leq \theta < 2\pi\}. \quad (9)$$

Both $\mathbf{M}_\lambda$ and $\mathbf{M}_v$ are 2D, and their structures can be understood in a rather intuitive fashion. A second-order tensor field $T(\mathbf{p})$ defined on a 2D manifold $\mathbf{M}$ introduces the following *continuous* maps:

$$\zeta_T : \mathbf{M} \to \mathbf{M}_\lambda, \quad \eta_T : \mathbf{M} \to \mathbf{M}_v. \quad (10)$$

In the next two sections, we describe the analysis of $\mathbf{M}_\lambda$ and $\mathbf{M}_v$.

4.1 Eigenvector Manifold

The analysis on eigenvectors and dual-eigenvectors by Zheng and Pang [40] can be largely summarized by (3)-(6). The eigenvector manifold presented here not only allows us to provide more geometric (intuitive) reconstruction of their results but also leads to novel analysis that includes the classification of degenerate points, extension of the Poincaré-Hopf theorem to 2D asymmetric tensor fields, and definition of pseudoeigenvectors which we use to visualize tensor structures in the complex domains. We begin with the definition of the eigenvector manifold.

The eigenvectors of an asymmetric tensor expressed in the form of (7) only depend on γ_r, γ_s, and θ. Given that the tensor magnitude and the isotropic scaling component do not affect the behaviors of eigenvectors, we will only
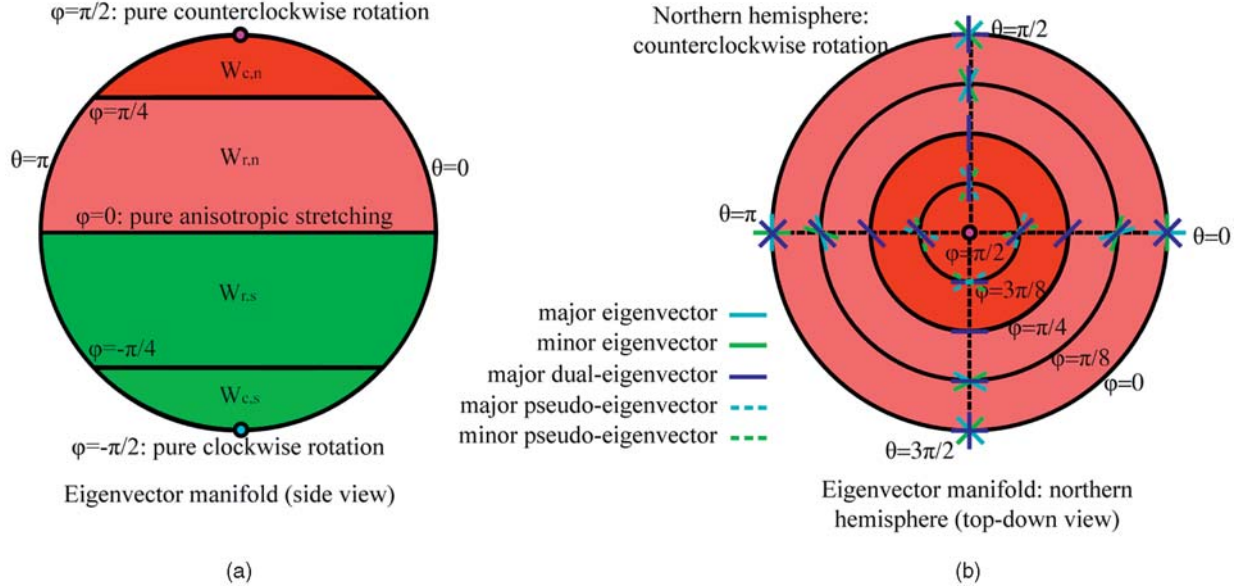
Fig. 2. (a) The eigenvector manifold is partitioned into real domains in the northern hemisphere ($W_{r,n}$) and the southern hemisphere ($W_{r,s}$) as well as complex domains in these hemispheres ($W_{c,n}$ and $W_{c,s}$). The orientation of the rotational component is counterclockwise in the northern hemisphere and clockwise in the southern hemisphere. The equator represents pure symmetric tensors, while the poles represent pure rotations. Along any longitude (e.g., (b) $\theta = 0$) and starting from the intersection with the equator and going north (b), the major dual-eigenvectors (blue lines) remain constant. In the real domains, i.e., $0 \leq \varphi < \frac{\pi}{4}$, the angle between the major eigenvectors (solid cyan lines) and the minor eigenvectors (solid green lines) monotonically decreases to 0. The angle is exactly 0 when the magnitude of the stretching constituent equals that of the rotational part. Inside the complex domains where major and minor eigenvectors are not real, pseudoeigenvectors (cyan and green dashed lines, details in Definition 4.6) are used for visualization purposes. The major and minor pseudoeigenvectors at φ ($\frac{\pi}{4} < \varphi < \frac{\pi}{2}$) are defined to be the same as the minor and major eigenvectors for $\frac{\pi}{2} - \varphi$ along the same longitude. Traveling south of the equator toward the south pole, the behaviors of the eigenvectors and pseudoeigenvectors are similar except they rotate in the opposite direction. At the equator, there are two bisectors, i.e., major and minor dual-eigenvectors cannot be distinguished. We consider the equator a bifurcation point and, therefore, part of tensor field features. On a different longitude, the same pattern repeats except the eigenvectors, dual-eigenvectors, and pseudoeigenvectors are rotated by a constant angle. Different longitudes correspond to different constant angles. Example vector fields are shown in Fig. 3.
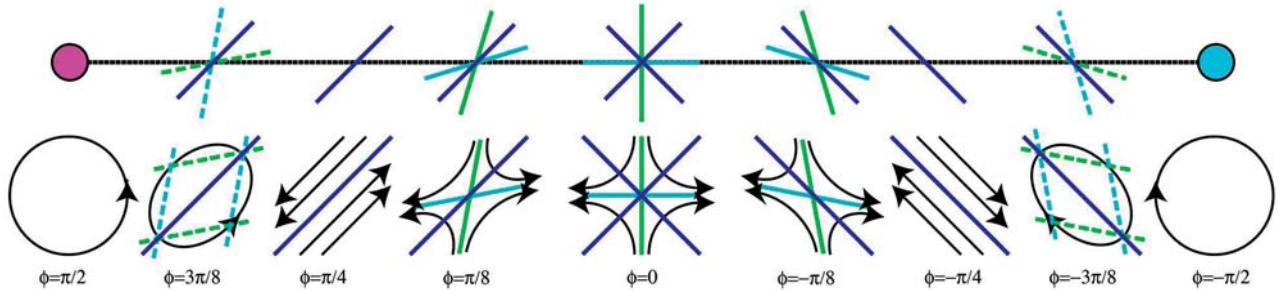

Fig. 3. Example vector fields whose gradient tensors correspond to points along the longitude $\theta = 0$ (Fig. 2b).

need to consider unit traceless tensors, i.e., $\gamma_d = 0$ and $\gamma_r^2 + \gamma_s^2 = 1$. They have the following form:

$$T(\theta, \varphi) = \sin \varphi \begin{pmatrix} 0 & -1 \\ 1 & 0 \end{pmatrix} + \cos \varphi \begin{pmatrix} \cos \theta & \sin \theta \\ \sin \theta & -\cos \theta \end{pmatrix}, \quad (11)$$

in which $\varphi = \arctan(\frac{\gamma_r}{\gamma_s}) \in [-\frac{\pi}{2}, \frac{\pi}{2}]$. Consequently, the set of unit traceless 2×2 tensors can be represented by a unit sphere which we refer to as the *eigenvector manifold* (Fig. 2a). The following observation provides some intuition about the eigenvector manifold:

Theorem 4.1. *Given two tensors $T_i = T(\theta_i, \varphi)$ ($i = 1, 2$) on the same latitude $-\frac{\pi}{2} < \varphi < \frac{\pi}{2}$, let*

$$N = \begin{pmatrix} \cos \delta & -\sin \delta \\ \sin \delta & \cos \delta \end{pmatrix}$$

with $\delta = \frac{\theta_2 - \theta_1}{2}$. Then, any eigenvector or dual-eigenvector $\overrightarrow{w_2}$ of T_2 can be written as $N \overrightarrow{w_1}$, where $\overrightarrow{w_1}$ is an eigenvector or dual-eigenvector of T_1, respectively.

The proofs of this theorem and the theorems thereafter are provided in the Appendix.

Theorem 4.1 states that, as one travels along a latitude in the eigenvector manifold, the eigenvectors and dual-eigenvectors are rotated at the same rate. This suggests that the fundamental behaviors of eigenvectors and dual-eigenvectors are dependent on φ only. In contrast, θ only impacts the directions of the eigenvectors and dual-eigenvectors, but not their relative positions (Fig. 2b).

Next, we will make use of the eigenvector manifold to provide a geometric construction of the dual-eigenvectors (Section 4.1.1), classify degenerate points and extend the

Poincaré-Hopf theorem to asymmetric tensor fields (Section 4.1.2), and introduce the pseudoeigenvectors that we use to illustrate tensor structures in the complex domains (Section 4.1.3).

4.1.1 Geometric Construction of Dual-Eigenvectors

Theorem 4.1 allows us to focus on the behaviors of eigenvectors and dual-eigenvectors along the longitude where $\theta = 0$, for which (11) reduces to

$$T = \begin{pmatrix} \cos\varphi & -\sin\varphi \\ \sin\varphi & -\cos\varphi \end{pmatrix}. \qquad (12)$$

The tensors have zero, one, or two real eigenvalues when $\cos 2\varphi < 0$, $= 0$, or > 0, respectively. Consequently, the tensor is referred to as being *in the complex domain*, *on a degenerate curve*, or *in the real domain* [40]. Notice that the tensor is on a degenerate curve if and only if $\varphi = \pm\frac{\pi}{4}$.

In the complex domains, it is straightforward to verify that $\binom{1}{1}$ and $\binom{1}{-1}$ are the dual-eigenvectors except when $\varphi = \pm\frac{\pi}{2}$, i.e., degenerate points. In the real domains, the eigenvalues are $\pm\sqrt{\cos 2\varphi}$. A major eigenvector is

$$\begin{pmatrix} \sqrt{\sin\left(\varphi + \frac{\pi}{4}\right)} + \sqrt{\cos\left(\varphi + \frac{\pi}{4}\right)} \\ \sqrt{\sin\left(\varphi + \frac{\pi}{4}\right)} - \sqrt{\cos\left(\varphi + \frac{\pi}{4}\right)} \end{pmatrix} \qquad (13)$$

and a minor eigenvector is

$$\begin{pmatrix} \sqrt{\sin\left(\varphi + \frac{\pi}{4}\right)} - \sqrt{\cos\left(\varphi + \frac{\pi}{4}\right)} \\ \sqrt{\sin\left(\varphi + \frac{\pi}{4}\right)} + \sqrt{\cos\left(\varphi + \frac{\pi}{4}\right)} \end{pmatrix}. \qquad (14)$$

The bisectors between them are lines $X = Y$ and $X = -Y$, where X and Y are the axes of the coordinate systems in the tangent plane at each point. That is, the dual-eigenvectors in the real domains are also $\binom{1}{1}$ and $\binom{1}{-1}$. Combined with the dual-eigenvector derivation in the complex domains, it is clear that the dual-eigenvectors remain the same for any $\varphi \in \left(-\frac{\pi}{2}, \frac{\pi}{2}\right)$. This is significant as it implies that the dual-eigenvectors depend primarily on the symmetric component of a tensor field.

The antisymmetric (rotational) component impacts the dual-eigenvectors in the following way: In the northern hemisphere where $\gamma_r = \sin\varphi > 0$, a major dual-eigenvector is $\binom{1}{1}$ and a minor dual-eigenvector is $\binom{1}{-1}$. In the southern hemisphere ($\gamma_r = \sin\varphi < 0$), the values of the dual-eigenvectors are swapped. Consequently, the major dual-eigenvector field J_1 is discontinuous across curves where $\varphi = 0$, which correspond to pure symmetric tensors (11) that form the boundaries between regions of counterclockwise rotations and regions of clockwise rotations.

With the help of Theorem 4.1, the above discussion can be formulated into the following:

Theorem 4.2. *The major and minor dual-eigenvectors of a tensor $T(\theta, \varphi)$ are, respectively, the major and minor eigenvectors of the following symmetric tensor:*

$$P_T = \frac{\gamma_r}{|\gamma_r|}\gamma_s \begin{pmatrix} \cos\left(\theta + \frac{\pi}{2}\right) & \sin\left(\theta + \frac{\pi}{2}\right) \\ \sin\left(\theta + \frac{\pi}{2}\right) & -\cos\left(\theta + \frac{\pi}{2}\right) \end{pmatrix}, \qquad (15)$$

wherever P_T is nondegenerate, i.e., $\gamma_r = \cos\varphi \neq 0$ and $\gamma_s = \sin\varphi \neq 0$.

This inspires us to incorporate places corresponding to $\varphi = 0$ into tensor field features in addition to $\varphi = \pm\frac{\pi}{4}$ (degenerate curves) and $\varphi = \pm\frac{\pi}{2}$ (degenerate points). Symmetric tensors and degenerate curves divide the eigenvector manifold $\mathbf{M}_v$ into four regions:

1. real domains in the northern hemisphere ($W_{r,n}$),
2. real domains in the southern hemisphere ($W_{r,s}$),
3. complex domains in the northern hemisphere ($W_{c,n}$), and
4. complex domains in the southern hemisphere ($W_{c,s}$).

Fig. 2a illustrates this partition.

Notice that φ measures the *signed* spherical distance of a unit traceless tensor to pure symmetric tensors (the equator). For example, the north pole has a positive distance and the south pole has a negative distance. In contrast, the circular discriminant Δ_2 (6) satisfies $\Delta_2 = 4\gamma_s$, which implies that Δ_2 does not make such a distinction between the two hemispheres. Therefore, we advocate the use of φ as a measure for the degree of being symmetric of an asymmetric tensor.

4.1.2 Degenerate Point Classification

Next, we discuss the degenerate points where dual-eigenvectors are undefined, i.e., circular points. We provide the following definition:

Definition 4.3. *Given a continuous asymmetric tensor field T defined on a 2D manifold $\mathbf{M}$, let Ω be a small circle around $\mathbf{p}_0 \in \mathbf{M}$ such that Ω contains no additional degenerate points and it encloses only one degenerate point, $\mathbf{p}_0$. Starting from a point on Ω and traveling counterclockwise along Ω, the major dual-eigenvector field (after normalization) covers the unit circle S^1 a number of times. This number is said to be the tensor index of $\mathbf{p}_0$ with respect to T, and is denoted by $I(\mathbf{p}_0, T)$.*

We now return to the discussion on degenerate points, which correspond to the poles ($\varphi = \pm\frac{\pi}{2}$), i.e., $\gamma_s = 0$. The relationship between the dual-eigenvectors of an asymmetric tensor $T(\theta, \varphi)$ and the corresponding symmetric tensor P_T described in (15) leads to the following theorem:

Theorem 4.4. *Let T be a continuous asymmetric tensor field defined on a 2D manifold $\mathbf{M}$ satisfying $\gamma_r^2 + \gamma_s^2 > 0$ everywhere in $\mathbf{M}$. Let S_T be the symmetric component of T which has a finite number of degenerate points $K = \{\mathbf{p}_i : 1 \leq i \leq N\}$. Then, we have the following:*

1. *K is also the set of degenerate points of T.*
2. *For any degenerate point $\mathbf{p}_i$, $I(\mathbf{p}_i, T) = I(\mathbf{p}_i, S_T)$. In particular, a wedge remains a wedge, and a trisector remains a trisector.*

This theorem allows us to not only detect degenerate points but also classify them based on their tensor indexes (wedges, trisectors, etc.) and the hemisphere they dwell on, something not addressed by Zheng and Pang's analysis [40]. Furthermore, this theorem leads directly to the extension of the well-known *Poincaré-Hopf theorem* for vector fields to asymmetric tensor fields as follows:
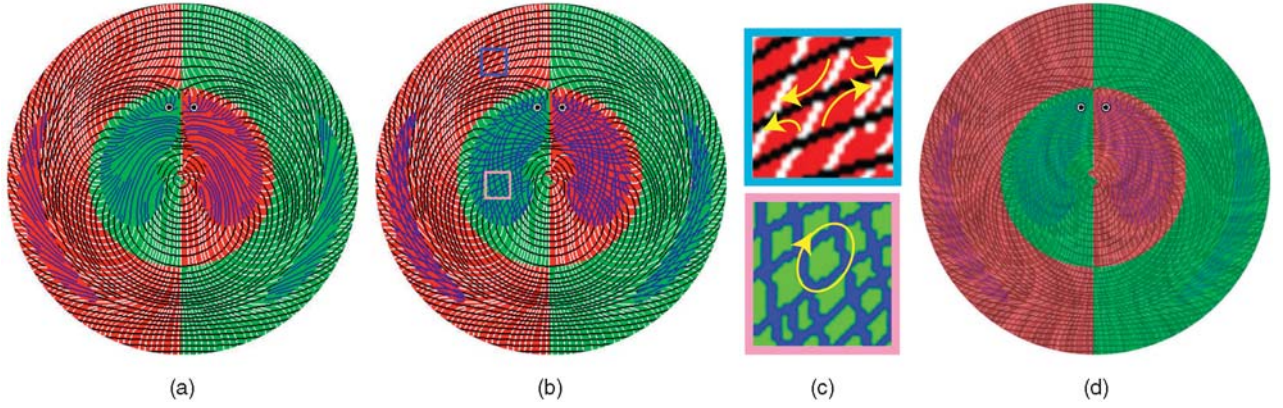
Fig. 4. Three tensor line-based techniques in visualizing the eigenvectors of the vector field shown in Fig. 1. In (a), the regions with a single family of tensor lines are the complex domains and the regions with two families of tensor lines are the real domains. Red indicates a counterclockwise rotational component, while green indicates a clockwise one. The major and minor eigenvectors (real domains) are colored black and white, respectively. The blue tensor lines inside the complex domains follow the major dual-eigenvectors. In (b), dual-eigenvectors are replaced by pseudoeigenvectors (blue) inside complex domains. The image in (d) is obtained from (b) by blending it with a texture-based visualization of the vector field. In (c), the physical meanings of eigenvectors (top) and pseudoeigenvectors (bottom) are annotated.

Theorem 4.5. *Let* $\mathbf{M}$ *be a closed orientable 2D manifold with an Euler characteristic* $\chi(\mathbf{M})$, *and let* T *be a continuous asymmetric tensor field with only isolated degenerate points* $\{\mathbf{p}_i : 1 \leq i \leq N\}$. *Then,*

$$\sum_{i=1}^{N} I(\mathbf{p}_i, T) = \chi(\mathbf{M}). \tag{16}$$

The eigenvector manifold also provides hints that degenerate points occurring at opposite poles have different rotational orientations. In fact, any tensor line connecting a degenerate point pair inside different hemispheres necessarily crosses the equator (pure symmetric tensors) an odd number of times. In contrast, when the degenerate point pair is in the same hemisphere, any connecting tensor line will cross the equator an even number of times or remain in the same hemisphere (zero crossing).

4.1.3 Pseudoeigenvectors

We conclude our eigenvector analysis with the introduction of pseudoeigenvectors, which like dual-eigenvectors, are continuous extensions of eigenvectors into the complex domains. Unlike dual-eigenvectors, however, pseudoeigenvectors are not mutually perpendicular. Recall that in the complex domains, flow patterns without translations and isotropic scalings are ellipses, whose elongated directions are represented by the major and minor dual-eigenvectors [40]. Unfortunately, the elliptical patterns cannot be demonstrated by drawing tensor lines following the major and minor dual-eigenvectors since they are always mutually perpendicular. To remedy this, we observe that an ellipse can be inferred from the smallest enclosing diamond whose diagonals represent the major and minor axes of the ellipse (Fig. 4c, bottom). Given two families of evenly spaced lines of the same density, d, intersecting at an angle $\alpha = f(\theta)$, any ellipse can be represented. Our question then is: Given a tensor $T(\theta, \varphi)$, where $\frac{\pi}{4} < |\varphi| < \frac{\pi}{2}$, how do we decide the directions of the two families of lines? This leads to the following definition:

Definition 4.6. *Given a tensor* $T = T(\theta, \varphi)$, *the* major pseudoeigenvector *of* T *is defined to be the* minor *eigenvector of the tensor* $T(\theta, \frac{\pi}{2} - \varphi)$ *when* $\varphi > \frac{\pi}{4}$ *and* $T(\theta, -\frac{\pi}{2} - \varphi)$ *when* $\varphi < -\frac{\pi}{4}$. *Similarly, the* minor pseudoeigenvector *of* T *is defined to be the* major *eigenvector of the same tensors under these conditions.*

It is straightforward to verify that evenly spaced lines following the major and minor pseudoeigenvectors produce diamonds whose smallest enclosing ellipses represent the flow patterns corresponding to T in the complex domains (Fig. 3: $\varphi = \pm \frac{3\pi}{8}$). Notice that the definitions of the major and minor pseudoeigenvectors can be swapped as evenly spaced lines following either definition produce the same diamonds. Because of this, we assign the same color (blue) to both pseudoeigenvector fields in our visualization techniques in which they are used (Figs. 4b and 4d).

Both major and minor pseudoeigenvector fields P_i ($i = 1, 2$) in the complex domains are continuous with respect to the major and minor eigenvector fields E_i ($i = 1, 2$) in the real domains across degenerate curves. Thus, we define the *major and minor augmented eigenvector fields* A_i ($i = 1, 2$) as

$$A_i(\mathbf{p}) = \begin{cases} E_i(\mathbf{p}) & T(\mathbf{p}) \text{ in the real domain,} \\ P_i(\mathbf{p}) & T(\mathbf{p}) \text{ in the complex domain.} \end{cases} \tag{17}$$

The major and minor pseudoeigenvectors are undefined at degenerate points, i.e., $\varphi = \pm \frac{\pi}{2}$. In fact, the set of degenerate points of either pseudoeigenvector field matches that of the major dual-eigenvector field (number, location, tensor index), thus respecting the adapted Poincaré-Hopf theorem for asymmetric tensor fields (Theorem 4.5). The orientations of tensor patterns in the pseudoeigenvector fields near degenerate points are obtained by rotating patterns in the major dual-eigenvector field in the same regions by $\frac{\pi}{4}$ either counterclockwise ($\varphi > 0$) or clockwise ($\varphi < 0$).

4.1.4 Visualizations

In Fig. 4, we apply three visualization techniques based on eigenvector analysis to the vector field shown in Fig. 1. In
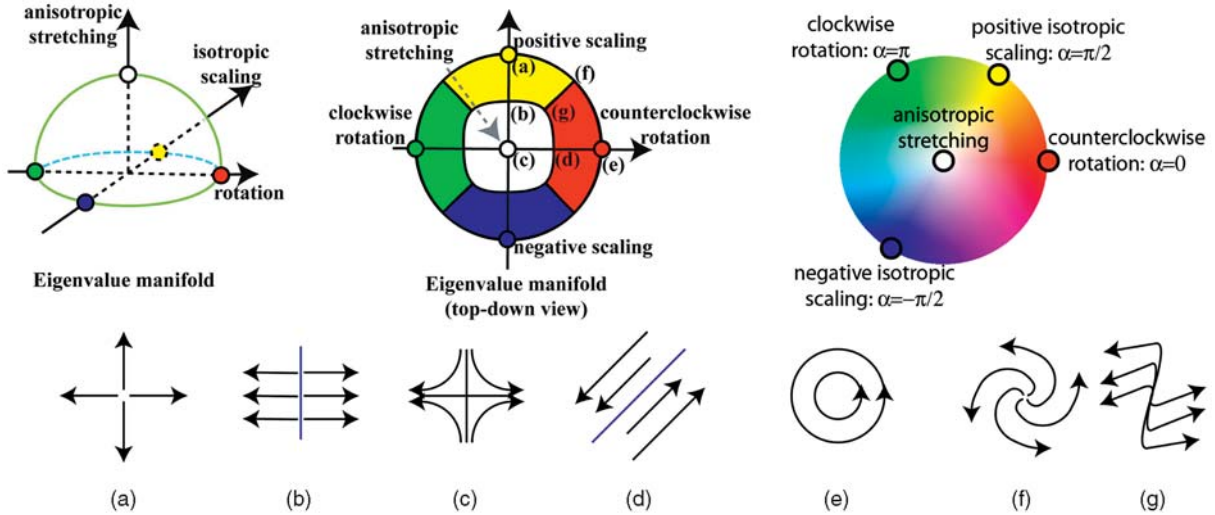
Fig. 5. The eigenvalue manifold of the set of 2×2 tensors. There are five special configurations (top-left: colored dots). The top-middle portion shows a top-down view of the hemisphere along the axis of anisotropic stretching. The hemisphere is decomposed into the Voronoi cells for the five special cases, where the boundary curves are part of tensor field features. To show the relationship between a vector field and the eigenvalues of the gradient, seven vector fields with constant gradient are shown in the bottom row: (a) $(\gamma_d, \gamma_r, \gamma_s) = (1, 0, 0)$, (b) $(\frac{\sqrt{2}}{2}, 0, \frac{\sqrt{2}}{2})$, (c) $(0, 0, 1)$, (d) $(0, \frac{\sqrt{2}}{2}, \frac{\sqrt{2}}{2})$, (e) $(0, 1, 0)$, (f) $(\frac{\sqrt{2}}{2}, \frac{\sqrt{2}}{2}, 0)$, and (g) $(\frac{\sqrt{3}}{3}, \frac{\sqrt{3}}{3}, \frac{\sqrt{3}}{3})$. Finally, we assign a unique color to every point in the eigenvalue manifold (upper-right). The boundary circle of the eigenvalue manifold is mapped to the loop of the hues. Notice the azimuthal distortion in this map, which is needed in order to assign positive and negative scaling with hues that are perceptually opposite. Similarly, we assign opposite hues to distinguish between counterclockwise and clockwise rotations.

addition to the option of visualizing eigenvectors in the real domains and major dual-eigenvectors in complex domains (Fig. 4a), pseudoeigenvectors provide an alternative (Fig. 4b). In these images, the background colors are either red (counterclockwise rotation) or green (clockwise rotation). Tensor lines following the major and minor eigenvector fields are colored in black and white, respectively. Tensor lines according to the dual-eigenvector field (Fig. 4a) and pseudoeigenvector fields (Fig. 4b) are colored in blue, which makes it easy to distinguish between real and complex domains. Degenerate points are highlighted as either black (wedges) or white (trisectors) disks. Note that it is easy to see the features of tensor fields (degenerate points, degenerate curves, purely symmetric tensors) in these visualization techniques. Fig. 4d overlays the eigenvector visualization in Fig. 4b onto texture-based visualization of the vector field. It is evident that flow directions do not align with the eigenvector or pseudoeigenvector directions. Furthermore, as expected, the fixed points in the vector field and degenerate points in the tensor field appear in different locations.

4.2 Eigenvalue Manifold

We now describe our analysis on the eigenvalues of 2×2 tensors, which have the following forms:

$$\lambda_{1,2} = \begin{cases} \gamma_d \pm \sqrt{\gamma_s^2 - \gamma_r^2} & \text{if } \gamma_s^2 \geq \gamma_r^2, \\ \gamma_d \pm i\sqrt{\gamma_r^2 - \gamma_s^2} & \text{if } \gamma_s^2 < \gamma_r^2. \end{cases} \quad (18)$$

Recall that γ_d, γ_r, and γ_s represent the (relative) strengths of the isotropic scaling, rotation, and anisotropic stretching components in the tensor field.

To understand the nature of a tensor usually requires the study of γ_d, γ_r, γ_s, or some of their combinations. Since no upper bounds on these quantities necessarily exist, the

effectiveness of the visualization techniques can be limited by the ratio between the maximum and minimum values. However, it is often desirable to answer the following questions:

- What are the relative strengths of the three components (γ_d, γ_r, and γ_s) at a point $\mathbf{p}_0$?
- Which of these components is dominant at $\mathbf{p}_0$?

Both questions are more concerned with the relative ratios among γ_d, γ_r, and γ_s rather than their individual values, which makes it possible to focus on unit tensors, i.e., when $\gamma_d^2 + \gamma_r^2 + \gamma_s^2 = 1$ and $\gamma_s \geq 0$. The set of all possible eigenvalue configurations satisfying these conditions can be modeled as a unit hemisphere, which is a compact 2D manifold (Fig. 5, upper-left).

There are five special points in the eigenvalue manifold that represent the extremal situations:

1. pure positive scaling ($\gamma_d = 1, \gamma_r = \gamma_s = 0$),
2. pure negative scaling ($\gamma_d = -1, \gamma_r = \gamma_s = 0$),
3. pure counterclockwise rotation ($\gamma_r = 1, \gamma_d = \gamma_s = 0$),
4. pure clockwise rotation ($\gamma_r = -1, \gamma_d = \gamma_s = 0$), and
5. pure anisotropic stretching ($\gamma_s = 1, \gamma_d = \gamma_r = 0$) (Fig. 5, upper-left).

The Voronoi diagram with respect to these configurations leads to a partition of the eigenvalue manifold into the following types of regions:

1. D^+ (positive scaling dominated),
2. D^- (negative scaling dominated),
3. R^+ (counterclockwise rotation dominated),
4. R^- (clockwise rotation dominated), and
5. S (anisotropic stretching dominated).

Here, the distance function is the spherical geodesic distance, i.e., $d(v_1, v_2) = 1 - v_1 \cdot v_2$ for any two points v_1
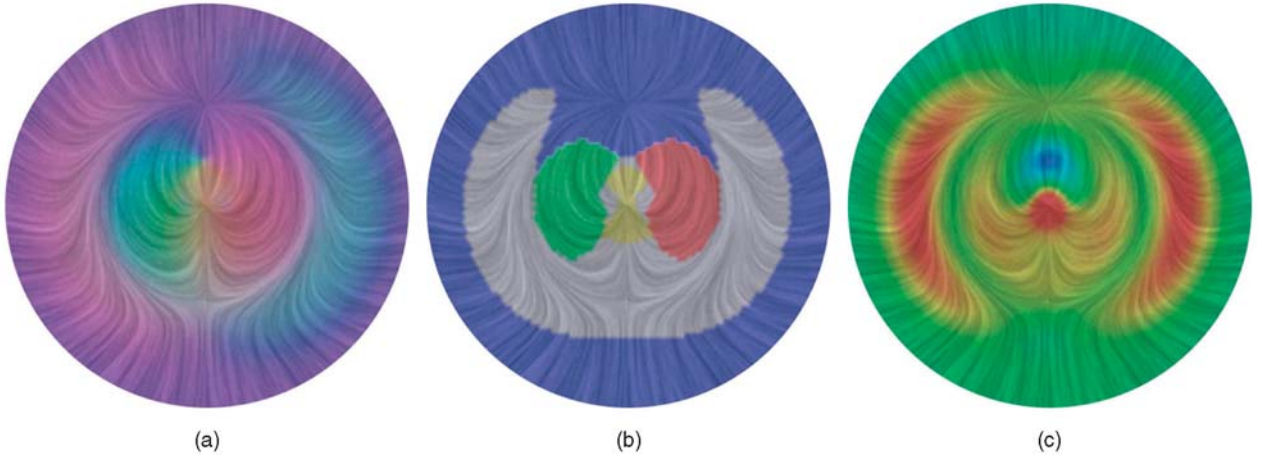
Fig. 6. Three visualization techniques on the vector field shown in Fig. 1 (Section 5.1): (a) eigenvalue visualization based on all components, (b) eigenvalue visualization based on the dominant component, and (c) magnitude (dyadic product) of the velocity gradient tensor. The color scheme for (a) is described in Fig. 5 (upper-right). The color scheme for (b) is based on the dominant component in the tensor: positive scaling (yellow), negative scaling (blue), counterclockwise rotation (red), clockwise rotation (green), and anisotropic stretching (white). In (c), red indicates large magnitudes and blue indicates small.

and v_2 on the eigenvalue manifold. The resulting diagram is illustrated in Fig. 5 (upper-middle).

A point $\mathbf{p}_0$ in the domain is said to be a type D^+ point if $T(\mathbf{p}_0)$ is in the Voronoi cell of pure positive scaling, i.e., $\gamma_d(\mathbf{p}_0) > \max(\gamma_s(\mathbf{p}_0), |\gamma_r(\mathbf{p}_0)|)$. A D^+-type region R is a connected region in which every point is of type D^+. Points and regions corresponding to the other types can be defined in a similar fashion. We define the features of a tensor field with respect to eigenvalues as the set of points in the domain whose tensor values map to the boundaries between the Voronoi cells in the eigenvalue manifold. The following result is a straightforward derivation from the Voronoi decomposition of the eigenvalue manifold:

Theorem 4.7. *Given a continuous asymmetric tensor field T defined on a 2D manifold $\mathbf{M}$, let U_1 and U_2 be α- and β-type regions, respectively, where $\alpha, \beta \in \{D^+, D^-, R^+, R^-, S\}$ are different. Then, $\partial U_1 \bigcap \partial U_2 = \emptyset$ if α- and β-types represent regions in the eigenvalue manifold that do not share a common boundary.*

As an application of this theorem, we state that a continuous path traveling from an R^+-type region to an R^--type region must intersect with a D^+-, D^--, or S-type region. A similar statement can be made between a D^+- and D^--type region pair. Note these statements can be difficult to verify without the use of eigenvalue manifold.

We propose two visualization techniques. With the first technique, we assign a unique color to each of the five special configurations shown in Fig. 5 (upper-middle). Effective color assignment can allow the user to identify the type of primary characteristics at a given point as well as the relative ratios among the three components. We use the scheme shown in Fig. 5 (upper-right): pure positive isotropic scaling (yellow), pure negative isotropic scaling (blue), pure counterclockwise rotation (red), pure clockwise rotation (green), and pure anisotropic stretching (white). For any other point $(\gamma_d(x,y), \gamma_r(x,y), \gamma_s(x,y))$, we compute α as the angular component of the vector $(\gamma_d(x,y), \gamma_r(x,y))$

with respect to $(1, 0)$ (counterclockwise rotation). The hue of the color is then

$$\begin{cases} \frac{2}{3}\alpha & \text{if } 0 \leq \alpha < \pi, \\ \frac{4}{3}\alpha & \text{if } -\pi \leq \alpha < 0. \end{cases} \quad (19)$$

Notice that angular distortion ensures that the two isotropic scalings and rotations will be assigned opposite colors, respectively. Our color legend is adopted from Ware [35]. The saturation of the color reflects $\gamma_d^2(x,y) + \gamma_r^2(x,y)$, and the value of the color is always one. This ensures that as the amount of anisotropic stretching increases, the color gradually changes to white, which is consistent with our choice of color for representing anisotropic stretching. Fig. 6a illustrates this visualization with the vector field shown in Fig. 1.

Our second eigenvalue visualization method assigns a unique color to each of the five Voronoi cells in the eigenvalue manifold. Fig. 6b shows this visualization technique for the aforementioned vector field.

Notice that the two techniques differ in how they address the transitions between regions of different dominant characteristics. The first method allows for smooth transitions and preserves relative strengths of γ_d, γ_r, and γ_s, which we refer to as the all components (AC) method. The second method explicitly illustrates the boundaries between regions with different dominant behaviors, which we refer to as the dominant component (DC) method. We use both methods in our interpretations of the data sets (Section 5). To illustrate the absolute magnitude of the tensor field, we provide a visualization in which the colors represent the magnitude of the gradient tensor, i.e., $\gamma_d^2 + \gamma_r^2 + \gamma_s^2$ (Fig. 6c). In this visualization, red indicates high values and blues indicate low values. Notice that this visualization can provide more complementary information than either the AC or DC method.

Combining visualizations based on eigenvalue and eigenvector analysis leads to several hybrid techniques. The following provides some insight on the link between eigenvalue analysis and eigenvector analysis:
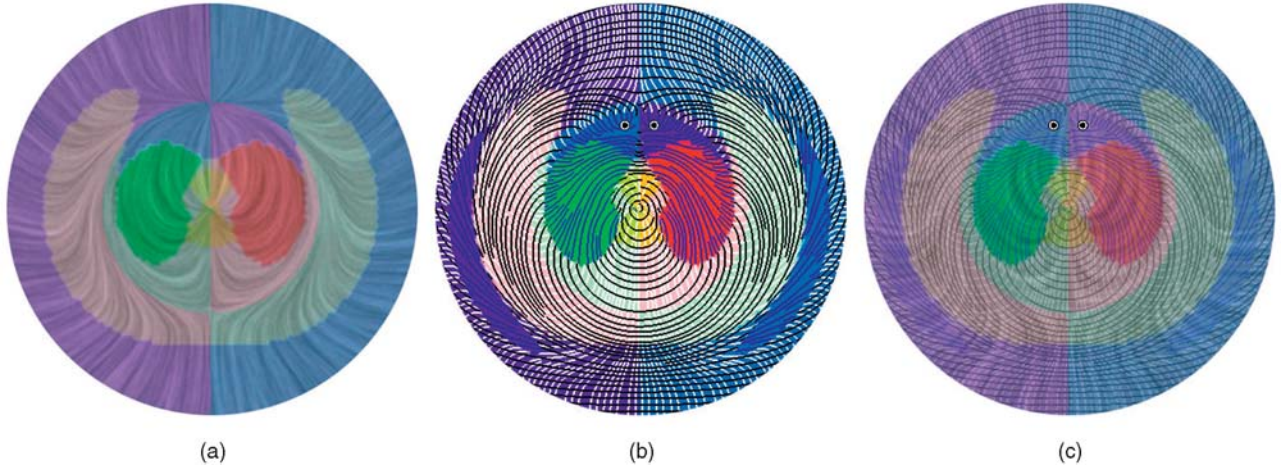
Fig. 7. Example hybrid visualization techniques on the vector field shown in Fig. 1: (a) a combination of eigenvalue-based visualization (Fig. 6b) with the background color (red and green) from eigenvector-based visualization (Fig. 4a), (b) same as (a) except the underlying texture-based vector field visualization is replaced by eigenvectors and major dual-eigenvectors, and (c) a combination of (a) and (b).

Theorem 4.8. *Given a continuous asymmetric tensor field T defined on a 2D manifold such that $\gamma_d^2 + \gamma_r^2 + \gamma_s^2 > 0$ everywhere, the following are true:*

1. *an R^+-type region is contained in $W_{c,n}$ and an R^--type region is contained in $W_{c,s}$,*
2. *an S-type region is contained in $W_{r,n} \bigcup W_{r,s}$, and*
3. *a D^+-type or D^--type region can have a nonempty intersection with any of the following: $W_{r,n}$, $W_{r,s}$, $W_{c,n}$, and $W_{c,s}$.*

Three hybrid visualizations are shown in Fig. 7. In Fig. 7a, the colors are obtained by combining the colors from the eigenvalue visualization (Fig. 6b) with the background colors (red or green) from eigenvector visualization (Fig. 4a). This results in eight different colors according to Theorem 4.8):

- $C_1 = R^+ \bigcap W_{c,n}$ (red),
- $C_2 = R^- \bigcap W_{c,s}$ (green),
- $C_3 = D^+ \bigcap (W_{c,n} \bigcup W_{r,n})$ (yellow + red),
- $C_4 = D^+ \bigcap (W_{c,s} \bigcup W_{r,s})$ (yellow + green),
- $C_5 = D^- \bigcap (W_{c,n} \bigcup W_{r,n})$ (blue + red),
- $C_6 = D^- \bigcap (W_{c,s} \bigcup W_{r,s})$ (blue + green),
- $C_7 = S \bigcap W_{r,n}$ (white + red), and
- $C_8 = S \bigcap W_{r,s}$ (white + green).

Furthermore, C_3-C_6 can be in either the real or complex domain. This can be distinguished based on the colors of the tensor lines (see Fig. 7b): real domains (tensor lines in black and white) and complex domains (tensor lines in blue). Fig. 7c is obtained by combining the visualizations in Figs. 7a and 7b.

4.3 Computation of Field Parameters

Our system can accept either a tensor field or a vector field. In the latter case, the vector gradient (a tensor) is used as the input. The computational domain is a triangular mesh in either a planar domain or a curved surface. The vector or tensor field is defined at the vertices only. To obtain values at a point on the edge or inside a triangle, we use a piecewise interpolation scheme. On surfaces, we use the scheme of Zhang et al. [37], [36] that ensures vector and

tensor field continuity in spite of the discontinuity in the surface normal.

Given a tensor field T, we first perform the following computation for every vertex:

- Reparameterization, in which we compute γ_d, γ_r, γ_s, and θ.
- Normalization, in which we scale γ_d, γ_r, and γ_s to ensure $\gamma_d^2 + \gamma_r^2 + \gamma_s^2 = 1$.
- Eigenvector analysis, in which we extract the eigenvectors, dual-eigenvectors, and pseudoeigenvectors at each vertex.

Next, we extract the features of the tensor field with respect to the eigenvalues. This is done by visiting every edge in the mesh to locate possible intersection points with the boundary curves of the Voronoi cells shown in Fig. 5. We then connect the intersection points whenever appropriate.

Finally, we extract tensor features based on eigenvectors. This includes the detection and classification of degenerate points as well as the extraction of degenerate curves and symmetric tensors.

5 PHYSICAL INTERPRETATION AND APPLICATIONS

In this section, we describe the physical interpretation of our asymmetric tensor analysis in the context of fluid flow fields. Let u be the flow velocity. The velocity gradient tensor ∇u consists of all the possible fluid motions except translation and can be decomposed into three terms [2], [28]:

$$\nabla u = \frac{\text{trace}[\nabla u]}{N}\delta_{ij} + \Omega_{ij} + E_{ij}, \qquad (20)$$

where δ_{ij} is the *Kronecker delta*, N is the dimension of the domain (either 2 or 3), $\frac{\text{trace}[\nabla u]}{N}\delta_{ij}$ represents the volume distortion (equivalent to *isotropic scaling* in mathematical terms), and the antisymmetric tensor $\Omega_{ij} = \frac{1}{2}(\nabla u - (\nabla u)^T)$ represents the averaged rotation of fluid. Since Ω_{ij} has only three entities when $N = 3$, it can be considered as a

pseudovector; twice the magnitude of the vector is called *vorticity*. The symmetric tensor

$$E_{ij} = \frac{1}{2}(\nabla u + (\nabla u)^T) - \frac{\text{trace}[\nabla u]}{N}\delta_{ij} \quad (21)$$

is termed the *rate-of-strain tensor* (or *deformation tensor*) that represents the angular deformation, i.e., the stretching of a fluid element along a principle axis. Notice that, in 2D cases, $(N = 2)$ (20) corresponds directly to the tensor reparameterization (7) in which $\gamma_d = \frac{\text{trace}[\nabla u]}{N}$, $\gamma_r = |\Omega_{12}|$, $\gamma_s = \sqrt{E_{11}^2 + E_{12}^2}$, and $\theta = \tan^{-1}(\frac{E_{12}}{E_{11}})$. Considering the gradient tensor of a 2D flow field (see Figs. 6 and 7 for an example), the counterclockwise and clockwise rotations in the tensor field indicate positive vorticities (red) and negative vorticities (green), respectively. The positive and negative isotropic scalings represent volumetric expansion and contraction of the fluid elements (yellow and blue). The anisotropic stretching is equivalent to the rate of angular deformation, i.e., shear strain (white). Furthermore, as illustrated in Fig. 3, eigenvectors in the real domain represent deformation patterns of fluid elements, while dual-eigenvectors in the complex domain represent the skewed (elliptical) rotation pattern.

For the analysis of 3D incompressible-fluid flows $(\sum_{i=1}^3 T_{ii} = 0)$ confined to a plane (e.g., Figs. 6 and 7), twice the trace of ∇u can be written as $T_{11} + T_{22} = -T_{33}$, which represents the net flow to the plane from neighboring planes: This is a consequence of mass conservation. Positive scaling in the plane represents the effect of inflow from the 3D neighborhood of the plane. This can also be interpreted as negative stretching of fluid material in the normal direction, i.e., the velocity gradient in the direction normal to the plane is negative $(T_{33} < 0)$. A similar interpretation can be made for negative scaling $(T_{33} > 0)$. For compressible fluids, the interpretation requires care. For example, positive scaling can not only represent volumetric dilation of compressible fluid but also contain the foregoing effect of inflow of the fluid from the neighborhood of the subject plane.

5.1 Sullivan Vortex: A Three Dimensional Flow

The first example we discuss is an analytical 3D incompressible flow that is presented by Sullivan [30]. This is an exact solution of the Navier-Stokes equations for a 3D vortex. The flow is characterized by

$$u_r(x,y,z)\begin{pmatrix}\cos\theta\\\sin\theta\\0\end{pmatrix} + u_\theta(x,y,z)\begin{pmatrix}-\sin\theta\\\cos\theta\\0\end{pmatrix}\\ + u_z(x,y,z)\begin{pmatrix}0\\0\\1\end{pmatrix}, \quad (22)$$

in which

$$\begin{aligned}u_r &= -ar + 6(\nu/r)[1 - e^{-(ar^2/2\nu)}],\\ u_\theta &= (\Gamma/2\pi r)[H(ar^2/2\nu)/H(\infty)],\\ u_z &= 2az[1 - 3e^{-ar^2/2\nu}]\end{aligned} \quad (23)$$
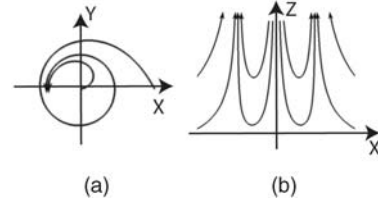

Fig. 8. The Sullivan Vortex viewed in (a) the x-y plane and (b) the x-z plane.

are the radial, azimuthal, and axial velocity components, respectively. Here, a (flow strength), Γ (flow circulation), and ν (kinematic viscosity) are constants, $r = \sqrt{x^2 + y^2}$, and

$$H(s) = \int_0^s \exp\left\{-t + 3\int_0^t \frac{1 - e^{-\tau}}{\tau}d\tau\right\}dt. \quad (24)$$

Sketches of the flow pattern in the horizontal and vertical planes are shown in Fig. 8. Away from the vortex center $r \to \infty$, the flow is predominantly in the negative radial direction (toward the center) with the accelerating upward flow: $u_r \approx -ar$, $u_\theta \approx 0$, $u_z \approx 2az$. On the other hand, as r becomes small $(r \to 0)$, we have $u_r \approx 3ar$, $u_\theta \approx 0$, $u_z \approx -4az$. Fig. 9 visualizes one instance of the Sullivan Vortex with $a = 1.5$, $\Gamma = 25$, and $\nu = 0.1$ in the plane $z = 1$.

Fig. 9a shows the velocity vector field together with the topology [4] identifying the unstable focus (the green dot) and the periodic orbit (the red loop). The images in Figs. 9b and 9c are the eigenvalue visualizations based on all components (AC method) and on the dominant component (DC method), respectively. The textures in Figs. 9b and 9c illustrate the major eigenvector field in the real domains and the major dual-eigenvector field in the complex domains. Due to the normalization of tensors, our visualization techniques shown in Figs. 9b and 9c exhibit relative strengths of tensor components (γ_d, γ_r, and γ_s) at a given point. To examine the absolute strength of velocity gradients in an inhomogeneous flow field, spatial variations of the magnitude (dyadic product) of velocity gradients are provided in Fig. 9d with the texture representing the velocity vector field. Red indicates high values and blue corresponds to low values.

The behaviors of the third dimension (z-direction) can be inferred from our DC-based eigenvalue visualization in the x-y plane (Fig. 9c). Namely, in the regions of large r, the negative isotropic scaling (blue) is dominant, and near the vortex center, the positive isotropic scaling (yellow) is dominant. Identifying such isotropic scaling is formidable with the use of texture-based vector visualization (Fig. 9a).

The eigenvalue visualization (Figs. 9b and 9c) allows us to see stretching-dominated regions (white), which cannot be identified from the corresponding vector field visualization (Fig. 9a). Figs. 9b and 9d collectively exhibit that strong counterclockwise rotation of fluid appears in the annular region near the center, and the rotation diminishes as r increases (away from the center). Notice that this information is difficult to extract from the texture-based vector visualization (Fig. 9a), although it can be achieved with a vorticity-based visualization.
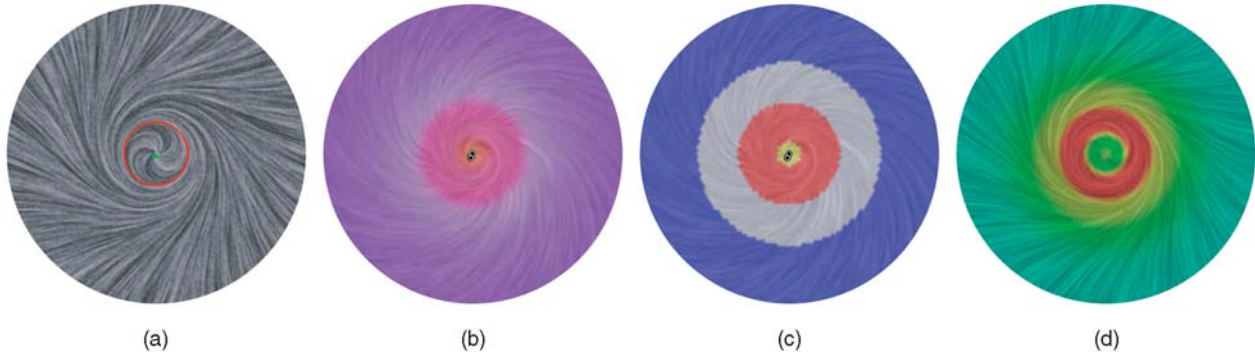
Fig. 9. Four visualization techniques on the Sullivan vortex: (a) vector field topology [4] with textures representing the velocity vector field, (b) eigenvalue visualization based on all components with textures showing major eigenvectors in the real domain and major dual-eigenvectors in the complex domain, (c) same as (b) except that colors encode the dominant component, and (d) magnitude (dyadic product) of the velocity gradient tensor with the underlying textures following the vector field. The visualization domain is $r \leq 2.667$.

Comparing the texture plots of Figs. 9a and 9b, we notice that the major eigenvectors (Fig. 9b: the directions of stretching) closely align with the streamlines in the real domain (Fig. 9a) for large enough r, while the major dual-eigenvectors (Fig. 9b: the direction of elongation) are nearly perpendicular to the streamlines (Fig. 9a) in the complex domain near the center of the vortex. This kind of enlightening observation is not revealed without tensor analysis.

The extremely localized high magnitude of velocity gradient (red region) shown in Fig. 9d represents the complex flows that resemble the *eye wall* of a hurricane or tornado, although, for large r, the Sullivan Vortex differs from hurricane or tornado flows.

We have also applied our visualization techniques to the combination of two Sullivan Vortices whose centers are slightly displaced with a distance of 0.17 and whose rotations are opposite but of equal strength. The visualization results are shown in Figs. 1, 4, 6, and 7.

5.2   Heat Transfer with a Cooling Jacket

A cooling jacket is used to keep an engine from overheating. Primary considerations for its design include

1. achieving an even distribution of flow to each cylinder,
2. minimizing pressure loss between the inlet and outlet,
3. eliminating flow stagnation, and
4. avoiding high-velocity regions that may cause bubbles or cavitation.

Fig. 10 shows the geometry of a cooling jacket, which consists of three components: 1) the lower half of the jacket or cylinder block, 2) the upper half of the jacket or cylinder head, and 3) the gaskets to connect the cylinder block to the head. Evidently, the geometry of the surface is highly complex.

In order to achieve efficient heat transfer from the engine block to the fluid flowing in the jacket, the fluid must be continuously convected while being mixed. Consequently, desirable flow patterns to enhance cooling include stretching and scaling that appear on the contact (inner) surface. As discussed earlier, stretching is a measure of fluid mixing. It increases the interfacial area

of a lump of fluid material, and the interfacial area is where heat exchange takes place by conduction. Given that the flow in the cooling jacket is considered incompressible [18], scalings that appear on the contact surface, whether positive or negative, indicate the flow components normal to the interface, i.e., convection at the interface. Note that fluid rotations (either counterclockwise or clockwise) would yield inefficient heat transfer at the contact interface since rotating motions do not increase the surface of a lump of fluid material and consequently do not contribute to the increase of mixing of fluids.

This data set has been examined using various vector field visualization techniques based on velocity and vorticity [22], [18], [19]. We have applied our asymmetric tensor analysis to this data set and discuss the additional insight that has not been observed from previous studies.

In order to distinguish the regions of rotation-dominant flows from scalings and anisotropic stretching, we choose to use the DC-based eigenvalue visualization (Fig. 11). In Figs. 11a and 11b, we show the outer and inner surface of the right half of the jacket, respectively. The visualization suggests that the flows are indicative of heat transfer, especially at the inner side of the wall (Fig. 11b). This is
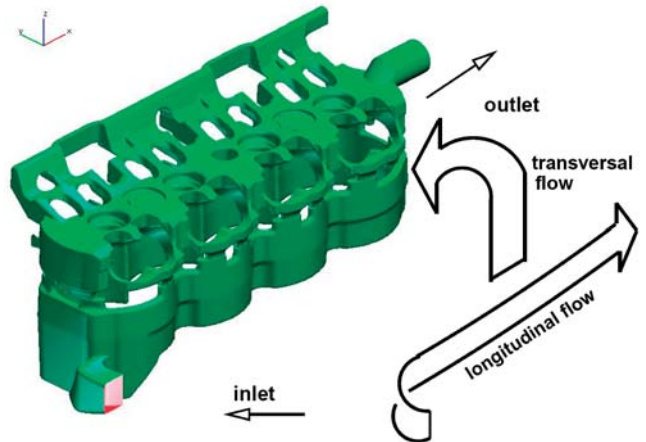

Fig. 10. The major components of the flow through a cooling jacket include a longitudinal component, lengthwise along the geometry, and a transversal component in the upward-and-over direction. The inlet and outlet of the cooling jacket are also indicated.
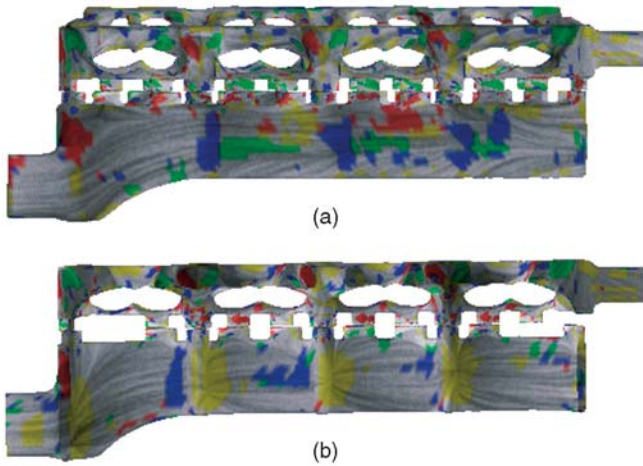
Fig. 11. DC-based (dominant component) eigenvalue visualization of a simulated flow field inside the cooling jacket: (a) the outside surface of a side wall in the cooling jacket and (b) the inside surface of the same side wall.

because a large portion of the surface area exhibits positive scaling (yellow), negative scaling (blue), and anisotropic stretching (white), whereas the area of predominant rotations (red and green) are relatively small. Comparing the inner and outer surfaces of the cooling jacket provides interesting insight into the flow patterns. In the cylinder blocks between the adjacent cylinders, the flow pattern in the inner surface (Fig. 11b) is positive scaling (yellow) preceded by negative scaling flows (blue), which represents the flows normal toward and away from the contact surface, respectively. The flow path from one cylinder to another has significant curvature (Fig. 10), and a portion of the flow is brought to the upper jacket through the gasket. It appears that curvature-induced advective deceleration and acceleration and the outflow to the upper jacket are responsible for the repetitious flow pattern on the inner surface. On the other hand, no clear repetitious pattern is present on the outer surface except negative scaling (blue) between the cylinders. In general, there is no significant region where flow rotation is dominant on the inner surface. While there are more rotation-dominated regions on the outer surface, it is not as critical as the inner surface. This indicates a positive aspect of the cooling jacket design.

While these flow patterns could be interpreted with vector field visualization, it would require a more careful inspection. On the other hand, our eigenvalue presentation of the tensor field can reveal such characteristics explicitly, automatically, and objectively. For example, to our knowledge, the aforementioned repeating patterns of positive and negative scalings on the inner surface (Fig. 11b), which are the flow characteristics normal to the surface, have not been reported from previous visualization work that studies this data set [22], [18], [19].

5.3 In-Cylinder Flow Inside a Diesel Engine

Swirl motion, an ideal flow pattern strived for in a diesel engine [23], resembles a helix spiral about an imaginary axis aligned with the combustion chamber as illustrated in Fig. 12. Achieving this ideal motion results in an optimal mixing of air and fuel and, thus, a more efficient
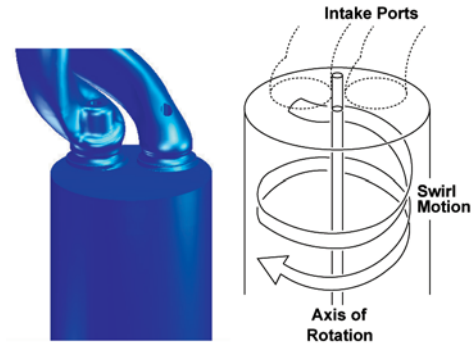

Fig. 12. The swirling motion of flow in the combustion chamber of a diesel engine. *Swirl* is used to describe circulation about the cylinder axis. The intake ports at the top provide the tangential component of the flow necessary for swirl. The data set consists of 776,000 unstructured adaptive resolution grid cells.

combustion process. A number of vector field visualization techniques have been applied to a simulated flow inside the diesel engine [23], [11], [4]. These techniques include arrow plots, color-coding velocity, textures, streamlines, vector field topology, and tracing particles. We have applied our tensor-based techniques to this data set, which, to our knowledge, is the first time asymmetric tensor analysis has been applied to this data.

Visualization of both eigenvalues and eigenvectors on the curved surface is presented in Fig. 13a (AC-based eigenvalue visualization) and Fig. 13b (a hybrid approach with eigenvectors and pseudoeigenvectors illustrated). We also apply our visualization techniques to a planar vector field obtained from a cross section of the cylinder at 25 percent of the length of the cylinder from the top where the intake ports meet the chamber. The visualization techniques are: (Fig. 13c) AC-based eigenvalue visualization, and (Fig. 13d) DC-based eigenvalue combined with eigenvectors and major dual-eigenvectors. Note that the textures shown in Figs. 13a and 13c illustrate the velocity vector field.

Figs. 13a and 13b demonstrate our technique for visualizing both eigenvalues and eigenvectors on a *curved* surface. The major eigenvectors in the real domain (stretching direction of fluid) do not align with the velocity vector streamlines. In some locations, they are perpendicular to each other. On the other hand, the elongation of rotating motion tends to be in a similar direction to the velocity vector (see Fig. 3 for the stretching and elongation interpretations in eigenvectors). Note that the trend is opposite to that of the Sullivan Vortex (Fig. 9). Also observe that the major eigenvectors appear aligned normal to the bottom surface that represents the piston head; this indicates that the diesel engine is in the intake process, hence, the flow is being stretched along the piston motion.

On the cylinder surface shown in Figs. 13a and 13b, there are two dominant regions: counterclockwise rotation and anisotropic stretching. There are two smaller regions indicating flow divergence (positive scaling shown in yellow): the one near the top of the cylinder is consistent with the flow-attachment pattern shown in the velocity vector streamlines in Fig. 13a and the other is near the bottom (near the piston head). Also observed is a small
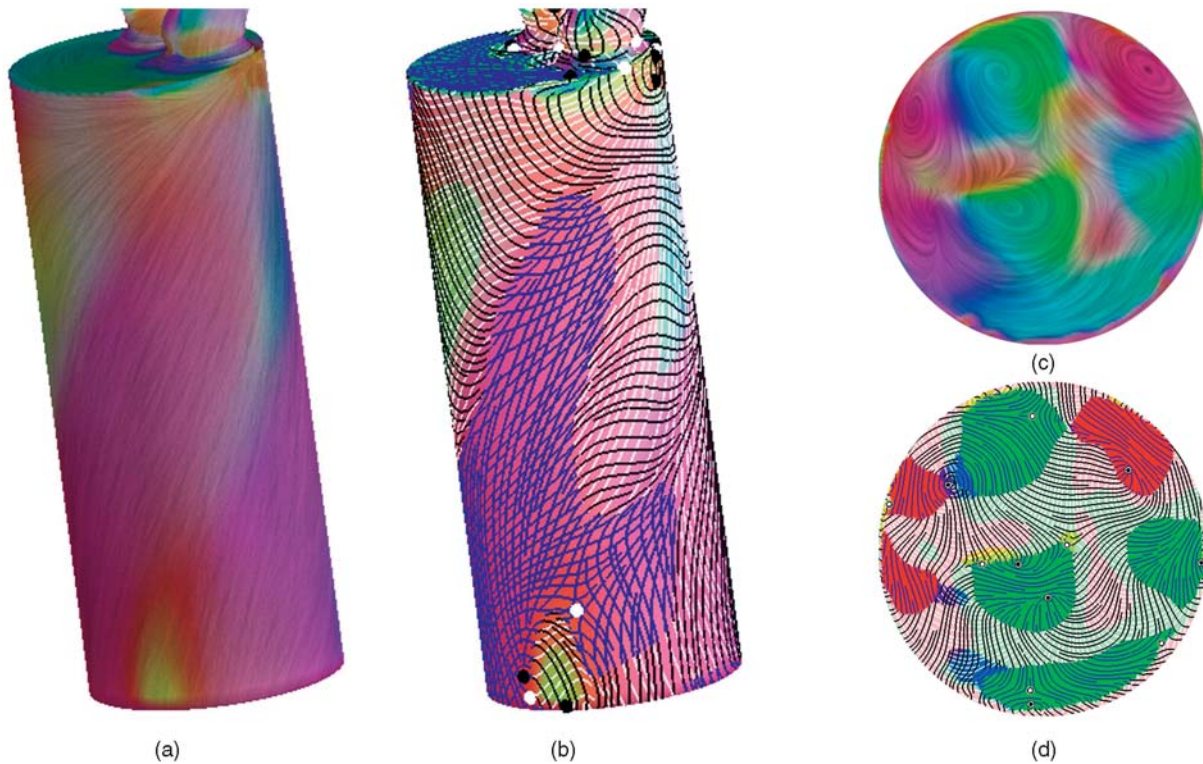
Fig. 13. Visualization of a diesel engine simulation data set: (a) AC-based (all components) eigenvalue visualization of the data on the surface of the engine, (b) hybrid eigenvalue and eigenvector visualization (Fig. 7b) of the gradient tensor on the surface with eigenvectors in the real domains and pseudoeigenvectors in the complex domains, (c) AC-based visualization of a planar slice (cut at 25 percent of the length of the cylinder from the top where the intake ports meet the chamber), and (d) the hybrid visualization used for (b) is applied to the planar slice. The degenerate points are highlighted using colored dots: black for wedges and white for trisectors.

region of negative scaling (shown in blue) along the right side edge that indicates inward flows from the wall. The alternating pattern of positive and negative scalings along the spiral motion is informative. On the other hand, the top of the cylinder shows the dominance of clockwise rotation, which is consistent with the spiral pattern. These observations are difficult to make from visualization of the velocity vector field, i.e., the texture in Fig. 13a alone.

The locations of pure circular rotation of fluid can be spotted in Fig. 13b as the degenerating points such as wedges (black dots) and trisectors (white dots). A degenerate point represents the location of zero angular strain. Hence, for 2D incompressible flows, no mixing or energy dissipation can take place at the degenerate points. Nonetheless, it is not exactly the case for 3D and compressible flows in this example, because stretching could still take place in the direction normal to the surface if an isotropic scaling component was present.

The vector plot of Fig. 13c shows the complex flow pattern comprising several vortices with both rotations. The complex pattern results from the decelerating flow, since this flow field is taken at the end of the intake process, i.e., the cylinder head is near the bottom. The overlay of eigenvalues effectively exhibits the directions of rotation, positive and negative isotropic scaling (expansion and contraction), and anisotropic stretching (shear strain).

In Fig. 13d, the direction of stretching is readily understood by the major and minor eigenvectors in the real domains and the major dual-eigenvectors in the complex

domains. This image also demonstrates the fact, as we showed in Figs. 2 and 5, that fluid rotation cannot directly come in contact with the flow of opposite rotational orientation. There must be a region of stretching in-between with the only exception being a pure source or sink. Furthermore, it can be observed that the regions between rotations in the same direction tend to induce stretching. The regions between rotations in the opposite directions tend to generate negative scaling, which represents volumetric contraction. There are several degenerate points such as wedges (black dots) and trisectors (white dots) in the figure.

In summary, the following flow characteristics are visualized for the diesel engine data set: expansion, contraction, stretching, elongation, and degenerate points. It is evident that significantly enriched flow interpretations can be achieved with the tensor visualization presented herein.

6   CONCLUSION AND FUTURE WORK

In this article, we provide the analysis of asymmetric tensor fields defined on 2D manifolds and develop effective visualization techniques based on such analysis. At the core of our technique is a novel parameterization of the space of 2×2 tensors, which has well-defined physical meanings when the tensors are the gradient of a vector field.

Based on the parameterization, we introduce the concepts of *eigenvalue manifold* (Fig. 5) and *eigenvector manifold* (Fig. 2) and describe the features of these objects. Analysis based on them leads to physically motivated partitions of

the flow field, which we exploit in order to construct visualization techniques. In addition, we provide a geometric characterization of the dual-eigenvectors (Theorem 4.2), an algorithm to classify degenerate points (Theorem 4.4), and the definition of pseudoeigenvectors (Definition 4.6) which we use to visualize tensor structures inside complex domains.

We provide a physical interpretation of our approach in the context of flow understanding, which is enabled by the relationship between our tensor parameterization and its physical interpretation. Our visualization techniques can provide a compact and concise presentation of flow kinematics. Principal motions of fluid material consist of angular deformation (i.e., stretching), dilation (i.e., scaling), rotation, and translation. In our tensor field visualization, the first three components (stretching, scaling, and rotation) are expressed explicitly, while the translational component is not illustrated. One of the advantages in our tensor visualization is that the kinematics expressed in eigenvalues and eigenvectors can be interpreted physically, for example, to identify the regions of efficient and inefficient mixing. Furthermore, the components of scaling (divergence and convergence) in a 2D surface for incompressible flows can provide information for the 3D flow; negative scaling represents stretching of fluid in the direction normal to the surface, and vice versa.

We demonstrate the efficiency of these visualization methods by applying them to the Sullivan Vortex, an exact solution to the Navier-Stokes equations, as well as two CFD simulation applications for a cooling jacket and a diesel engine.

To summarize, the eigenvalue visualization enables us to examine the relative strengths of fluid expansion (contraction), rotations, and the rate of shear strain in one single plot. Hence, such a plot is convenient for inspection of global flow characteristics and behaviors, as well as to detect salient features. In fact, the visualization technique should be ideal for the exploratory investigation of complex flow fields. Furthermore, the developed eigenvector visualization allows us to uniquely identify the detailed deformation patterns of the fluid, which provides additional insights in the understanding of fluid motions. Consequently, the tensor-based visualization techniques will provide an additional tool for flow-field investigations.

There are a number of possible future research directions that are promising. First, in this work, we have focused on a 2D subset of the full 3D eigenvalue manifold (unit tensors). While this allows an efficient segmentation of the flow based on the dominant component, the tensor magnitude can be used to distinguish between regions of the same dominant component but with significantly different total strengths (Fig. 6c). We plan to incorporate the absolute magnitude of the tensor field into our analysis and study the full 3D eigenvalue manifold. Second, tensor field simplification is an important task, and we will explore proper simplification operations and metrics that apply to asymmetric tensor fields. Third, we plan to expand our research into 3D domains as well as time-varying fields. For 3D fields, we will seek to explore the relationships between pure symmetric tensors and pure antisymmetric tensors

much like what we have done for the 2D case in this article. We also plan to extend ideas of eigenvalue and eigenvector manifolds to 3D flow fields.

APPENDIX

PROOFS

In this appendix, we provide the proofs for the theorems from Section 4.

Theorem 4.1. *Given two tensors $T_i = T(\theta_i, \varphi)$ $(i = 1, 2)$ on the same latitude $-\frac{\pi}{2} < \varphi < \frac{\pi}{2}$, let*

$$N = \begin{pmatrix} \cos \delta & -\sin \delta \\ \sin \delta & \cos \delta \end{pmatrix}$$

with $\delta = \frac{\theta_2 - \theta_1}{2}$. Then, any eigenvector or dual-eigenvector $\overrightarrow{w_2}$ of T_2 can be written as $N\overrightarrow{w_1}$, where $\overrightarrow{w_1}$ is an eigenvector or dual-eigenvector of T_1, respectively.

Proof. It is straightforward to verify that $T_2 = NT_1N^T$, i.e., T_1 and T_2 are *congruent*. Results from classical linear algebra state that T_1 and T_2 have the same set of eigenvalues. Furthermore, a vector $\overrightarrow{w_1}$ is an eigenvector of T_1 if and only if $\overrightarrow{w_2} = N\overrightarrow{w_1}$ is an eigenvector of T_2.

To verify the relationship between the dual-eigenvectors of T_1 and T_2, let

$$U_1 \begin{pmatrix} \mu_1 & 0 \\ 0 & \mu_2 \end{pmatrix} V_1$$

be the singular value decomposition of T_1. Then,

$$U_2 \begin{pmatrix} \mu_1 & 0 \\ 0 & \mu_2 \end{pmatrix} V_2$$

in which $U_2 = NU_1$ and $V_2 = V_1N^T$ is the singular decomposition of T_2. This implies that T_1 and T_2 have the same singular values μ_1 and μ_2.

The relationship between the dual-eigenvectors of T_1 and T_2 can be verified by plugging into (3) and (4) the aforementioned statements on eigenvectors and singular values between congruent matrices. □

Theorem 4.4. *Let T be a continuous asymmetric tensor field defined on a 2D manifold $\mathbf{M}$ satisfying $\gamma_r^2 + \gamma_s^2 > 0$ everywhere in $\mathbf{M}$. Let S_T be the symmetric component of T which has a finite number of degenerate points $K = \{\mathbf{p}_i : 1 \leq i \leq N\}$. Then, we have the following:*

1. *K is also the set of degenerate points of T.*
2. *For any degenerate point $\mathbf{p}_i$, $I(\mathbf{p}_i, T) = I(\mathbf{p}_i, S_T)$. In particular, a wedge remains a wedge and a trisector remains a trisector.*

Proof. Given that $\gamma_s^2(T) + \gamma_r^2(T) > 0$ everywhere in the domain, the degenerate points of T only occur inside complex domains. Recall that the structures of T inside complex domains are defined using the dual-eigenvectors, which are the eigenvectors of symmetric tensor field P_T (15). Moreover, the set of degenerate points of T is the same as the set of degenerate points of P_T inside complex domains, i.e., $\varphi = \pm\frac{\pi}{2}$.

Notice that the major and minor eigenvectors of P_T are obtained from corresponding eigenvectors of S_T by rotating them either counterclockwise or clockwise by $\frac{\pi}{4}$. Within each connected component in the complex domains, the orientation of the rotation is constant. Zhang et al. [36] show that rotating the eigenvectors of a symmetric tensor field (in this case, S_T) uniformly in the domain (in this case, a connected component of the complex domains) by an angle of β (in this case, $\pm \frac{\pi}{4}$) results in another symmetric tensor field that has the same set of degenerate points as the original field. Moreover, the tensor indices of the degenerate points are maintained by such rotation. Therefore, S_T and P_T (and consequently, T) have the same set of degenerate points. Furthermore, the tensor indices are the same between corresponding degenerate points. □

Theorem 4.5. *Let* **M** *be a closed orientable 2D manifold with an Euler characteristic* $\chi(\mathbf{M})$*, and let* T *be a continuous asymmetric tensor field with only isolated degenerate points* $\{\mathbf{p}_i : 1 \leq i \leq N\}$*. Then,*

$$\sum_{i=1}^{N} I(\mathbf{p}_i, T) = \chi(\mathbf{M}). \qquad (25)$$

Proof. $\sum_{i=1}^{N} I(\mathbf{p}_i, T) = \sum_{i=1}^{N} I(\mathbf{p}_i, S_T) = \chi(\mathbf{M})$. The first equation is a direct consequence of Theorem 4.4, while the second equation makes use of the fact that S_T is a symmetric tensor field, for which the *Poincaré-Hopf theorem* has been proven true [5]. □

Theorem 4.7. *Given a continuous asymmetric tensor field* T *defined on a 2D manifold* **M***, let* U_1 *and* U_2 *be an* α*- and* β*-type region, respectively, where* $\alpha, \beta \in \{D^+, D^-, R^+, R^-, S\}$ *are different. Then,* $\partial U_1 \bigcap \partial U_2 = \emptyset$ *if* α*- and* β*-types represent regions in the eigenvalue manifold that do not share a common boundary.*

Proof. Since ζ_T (10) is a continuous map from **M** to the eigenvalue manifold $\mathbf{M}_\lambda$, we have $\zeta_T^{-1}(\emptyset) = \emptyset$. □

Theorem 4.8. *Given a continuous asymmetric tensor field* T *defined on a 2D manifold such that* $\gamma_d^2 + \gamma_r^2 + \gamma_s^2 > 0$ *everywhere, the following are true:*

1. *an* R^+*-type region is contained in* $W_{c,n}$ *and an* R^-*-type region is contained in* $W_{c,s}$*,*
2. *an* S*-type region is contained in* $W_{r,n} \bigcup W_{r,s}$*, and*
3. *a* D^+*-type or* D^-*-type region can have a nonempty intersection with any of the following:* $W_{r,n}$*,* $W_{r,s}$*,* $W_{c,n}$*, and* $W_{c,s}$*.*

Proof. Given a point $\mathbf{p}_0$ in an R^+-type region, we have $\gamma_r(\mathbf{p}_0) > \gamma_s(\mathbf{p}_0) \geq 0$, i.e., $\mathbf{p}_0$ is in a complex domain in the northern hemisphere $(W_{c,n})$. Similarly, if $\mathbf{p}_0$ is in an R^--type region, then $\mathbf{p}_0 \in W_{c,s}$.

If $\mathbf{p}_0$ is in an S-type region, then $\gamma_s(\mathbf{p}_0) > |\gamma_r(\mathbf{p}_0)|$, i.e., $\mathbf{p}_0$ is in the real domains that can be in either the northern or the southern hemisphere.

Finally, if $\mathbf{p}_0$ is in a D^+-type region, then $\gamma_d(\mathbf{p}_0) > \max(|\gamma_r(\mathbf{p}_0)|, \gamma_s(\mathbf{p}_0))$. However, there is no constraint on the discriminant $\varphi = \arctan(\frac{\gamma_r}{\gamma_s})$. Therefore, $\mathbf{p}_0$ can be inside any of $W_{r,n}$, $W_{r,s}$, $W_{c,n}$, and $W_{c,s}$. A similar statement can be made when $\mathbf{p}_0$ is in a D^--type region. □

REFERENCES

[1] P. Alliez, D. Cohen-Steiner, O. Devillers, B. Lévy, and M. Desbrun, "Anisotropic Polygonal Remeshing," *ACM Trans. Graphics, Proc. ACM SIGGRAPH '03,* vol. 22, no. 3, pp. 485-493, July 2003.
[2] G.K. Batchelor, *An Introduction to Fluid Dynamics.* Cambridge Univ. Press, 1967.
[3] B. Cabral and L.C. Leedom, "Imaging Vector Fields Using Line Integral Convolution," *Proc. ACM SIGGRAPH '93,* Ann. Conf. Series, pp. 263-272, 1993.
[4] G. Chen, K. Mischaikow, R.S. Laramee, P. Pilarczyk, and E. Zhang, "Vector Field Editing and Periodic Orbit Extraction Using Morse Decomposition," *IEEE Trans. Visualization and Computer Graphics,* vol. 13, no. 4, pp. 769-785, July-Aug. 2007.
[5] T. Delmarcelle, "The Visualization of Second-Order Tensor Fields," PhD dissertation, Stanford Applied Physics, 1994.
[6] T. Delmarcelle and L. Hesselink, "Visualizing Second-Order Tensor Fields with Hyperstream Lines," *IEEE Computer Graphics and Applications,* vol. 13, no. 4, pp. 25-33, July 1993.
[7] T. Delmarcelle and L. Hesselink, "The Topology of Symmetric, Second-Order Tensor Fields," *Proc. Fifth IEEE Conf. Visualization (Vis),* 1994.
[8] J. Ebling and G. Scheuermann, "Clifford Convolution and Pattern Matching on Vector Fields," *Proc. 14th IEEE Conf. Visualization (Vis '03),* pp. 193-200, 2003.
[9] J. Ebling and G. Scheuermann, "Segmentation of Flow Fields Using Pattern Matching," *Proc. Eighth Joint Eurographics-IEEE VGTC Symp. Visualization (EuroVis '06),* pp. 147-154, 2006.
[10] H.B. Fischer, J. Imberger, E.J. List, R.C.Y. Koh, and N.H. Brooks, *Mixing in Inland and Coastal Waters.* Academic Press, 1979.
[11] C. Garth, R. Laramee, X. Tricoche, J. Schneider, and H. Hagen, "Extraction and Visualization of Swirl and Tumble Motion from Engine Simulation Data," *Proc. Topology-Based Methods in Visualization Workshop,* series Math. and Visualization, pp. 121-135, 2007.
[12] J.L. Helman and L. Hesselink, "Visualizing Vector Field Topology in Fluid Flows," *IEEE Computer Graphics and Applications,* vol. 11, no. 3, pp. 36-46, May 1991.
[13] L. Hesselink, Y. Levy, and Y. Lavin, "The Topology of Symmetric, Second-Order 3D Tensor Fields," *IEEE Trans. Visualization and Computer Graphics,* vol. 3, no. 1, pp. 1-11, Mar. 1997.
[14] M. Hlawitschka, J. Ebling, and G. Scheuermann, "Convolution and Fourier Transform of Second Order Tensor Fields," *Proc. Fourth IASTED Int'l Conf. Visualization, Imaging, and Image Processing (VIIP '04),* pp. 78-83, 2004.
[15] H. Hotz, L. Feng, H. Hagen, B. Hamann, K. Joy, and B. Jeremic, "Physically Based Methods for Tensor Field Visualization," *Proc. 15th IEEE Conf. Visualization (Vis '04),* pp. 123-130, 2004.
[16] J. Jeong and F. Hussain, "On the Identification of a Vortex," *J. Fluid Mechanics,* vol. 285, pp. 69-94, 1995.
[17] D.N. Kenwright, "Automatic Detection of Open and Closed Separation and Attachment Lines," *Proc. Ninth IEEE Conf. Visualization (Vis '98),* pp. 151-158, 1998.
[18] R.S. Laramee, C. Garth, H. Doleisch, J. Schneider, H. Hauser, and H. Hagen, "Visual Analysis and Exploration of Fluid Flow in a Cooling Jacket," *Proc. 16th IEEE Conf. Visualization (Vis '05),* pp. 623-630, 2005.
[19] R.S. Laramee, C. Garth, J. Schneider, and H. Hauser, "Texture-Advection on Stream Surfaces: A Novel Hybrid Visualization Applied to CFD Results," *Proc. Eighth Joint Eurographics-IEEE VGTC Symp. Visualization (EuroVis '06),* pp. 155-162, 2006.
[20] R.S. Laramee, H. Hauser, H. Doleisch, F.H. Post, B. Vrolijk, and D. Weiskopf, "The State of the Art in Flow Visualization: Dense and Texture-Based Techniques," *Computer Graphics Forum,* vol. 23, no. 2, pp. 203-221, June 2004.

[21] R.S. Laramee, H. Hauser, L. Zhao, and F.H. Post, "Topology Based Flow Visualization: The State of the Art," *Proc. Topology-Based Methods in Visualization Workshop (TopoInVis '05),* Visualization and Math., pp. 1-19, 2007.

[22] R.S. Laramee, J.J. van Wijk, B. Jobard, and H. Hauser, "ISA and IBFVS: Image Space Based Visualization of Flow on Surfaces," *IEEE Trans. Visualization and Computer Graphics,* vol. 10, no. 6, pp. 637-648, Nov. 2004.

[23] R.S. Laramee, D. Weiskopf, J. Schneider, and H. Hauser, "Investigating Swirl and Tumble Flow with a Comparison of Visualization Techniques," *Proc. 15th IEEE Conf. Visualization (Vis '04),* pp. 51-58, 2004.

[24] J.M. Ottino, *The Kinematics of Mixing: Stretching, Chaos and Transport.* Cambridge Univ. Press, 1989.

[25] R. Peikert and M. Roth, "The Parallel Vectors Operator—A Vector Field Visualization Primitive," *Proc. 10th IEEE Conf. Visualization (Vis '99),* pp. 263-270, 1999.

[26] M. Ruetten and M.S. Chong, "Analyzing Vortex Breakdown Flow Structures by Assignment of Colors to Tensor Invariants," *IEEE Trans. Visualization and Computer Graphics,* vol. 12, no. 5, pp. 1189-1196, 2006.

[27] I.A. Sadarjoen and F.H. Post, "Detection, Quantification, and Tracking of Vortices Using Streamline Geometry," *Computers and Graphics,* vol. 24, no. 3, pp. 333-341, June 2000.

[28] F. Sherman, *Viscous Flow.* McGraw-Hill, 1990.

[29] D. Sujudi and R. Haimes, "Identification of Swirling Flow in 3D Vector Fields," Technical Report AIAA Paper 95-1715, Am. Inst. Aeronautics and Astronautics, 1995.

[30] R.D. Sullivan, "A Two-Cell Vortex Solution of the Navier-Stokes Equations," *J. Aero/Space Sciences,* vol. 26, no. 11, pp. 767-768, Nov. 1959.

[31] X. Tricoche, G. Scheuermann, and H. Hagen, "Tensor Topology Tracking: A Visualization Method for Time-Dependent 2D Symmetric Tensor Fields," *Computer Graphics Forum,* Proc. Eurographics '01, vol. 20, no. 3, pp. 461-470, Sept. 2001.

[32] X. Tricoche, G. Scheuermann, and H. Hagen, *Topology Simplification of Symmetric, Second-Order 2D Tensor Fields, Hierarchical and Geometrical Methods in Scientific Visualization.* Springer, 2003.

[33] X. Tricoche, G. Scheuermann, H. Hagen, and S. Clauss, "Vector and Tensor Field Topology Simplification on Irregular Grids," *Proc. Joint Eurographics-IEEE TCVG Symp. Visualization (VisSym '01),* pp. 107-116, May 2001.

[34] J.J. van Wijk, "Image Based Flow Visualization," *ACM Trans. Graphics,* vol. 21, no. 3, pp. 745-754, 2002.

[35] C. Ware, *Information Visualization: Perception for Design,* second ed. Morgan Kaufmann, 2004.

[36] E. Zhang, J. Hays, and G. Turk, "Interactive Tensor Field Design and Visualization on Surfaces," *IEEE Trans. Visualization and Computer Graphics,* vol. 13, no. 1, pp. 94-107, 2007.

[37] E. Zhang, K. Mischaikow, and G. Turk, "Vector Field Design on Surfaces," *ACM Trans. Graphics,* vol. 25, no. 4, pp. 1294-1326, 2006.

[38] X. Zheng and A. Pang, "Hyperlic," *Proc. 14th IEEE Conf. Visualization (Vis '03),* pp. 249-256, 2003.

[39] X. Zheng and A. Pang, "Topological Lines in 3D Tensor Fields," *Proc. 15th IEEE Conf. Visualization (Vis '04),* pp. 313-320, 2004.

[40] X. Zheng and A. Pang, "2D Asymmetric Tensor Fields," *Proc. 16th IEEE Conf. Visualization (Vis '05),* pp. 3-10, 2005.

[41] X. Zheng, B. Parlett, and A. Pang, "Topological Structures of 3D Tensor Fields," *Proc. 16th IEEE Conf. Visualization (Vis '05),* pp. 551-558, 2005.

Eugene Zhang received the PhD degree in computer science from Georgia Institute of Technology, in 2004. He is currently an assistant professor at Oregon State University, where he is a faculty member in the School of Electrical Engineering and Computer Science. His research interests include computer graphics, scientific visualization, and geometric modeling. He received the National Science Foundation (NSF) CAREER award in 2006. He is a member of the IEEE.

Harry Yeh received the PhD degree in civil engineering from the University of California, Berkeley, in 1983. His research interests include the areas of environmental fluid mechanics, water wave phenomena, wind turbulence, and tsunami hazard mitigation. He was a hydraulic engineer at Bechtel Inc., San Francisco from 1977 to 1983. From 1983 to 2002, he was a professor at the University of Washington, Seattle. He is currently the Edwards chair professor in engineering at Oregon State University.

Zhongzang Lin received the BS degree from Zhejiang University, in 2006. He is currently working toward the PhD degree in computer science at Oregon State University. He is currently working with Eugene Zhang on tensor field analysis and visualization. His research interests include scientific visualization, computer graphics, and geometric modeling.

Robert S. Laramee received the bachelor's degree (cum laude) in physics from the University of Massachusetts, Amherst, in 1997, the master's degree in computer science from the University of New Hampshire, Durham, in 2000, and the PhD degree from the Vienna University of Technology, Vienna, in 2005. From 2001 to 2006, he was a researcher at the VRVis Research Center (www.vrvis.at) and a software engineer at AVL (www.avl.com), Department of Advanced Simulation Technologies. He is currently a lecturer (an assistant professor) in the Department of Computer Science, Swansea University (Prifysgol Cymru Abertawe), Wales. His research interests include the areas of scientific visualization, computer graphics, and human-computer interaction.